Dynamic Modeling of the Anisotropic Non-Ideal Gyroscopic Rotor System

Zharilkassin Iskakov * , Aziz Kamal , Assylbek Jomartov

Posted Date: 22 May 2026

doi: 10.20944/preprints202605.1561.v1

Keywords: gyroscopic rotary system; dynamic modeling; stiffness anisotropy; non-ideal source; Sommerfeld effect; non-linearity of damping

 doi:10.20944/preprints202605.1561.v1

Article

Dynamic Modeling of the Anisotropic Non-Ideal Gyroscopic Rotor System

Zharilkassin Iskakov *, Aziz Kamal and Assylbek Jomartov

Joldasbekov Institute of Mechanics and Engineering, Shevchenko Str., 28, Almaty 050010, Kazakhstan

* Correspondence: iskakov53@mail.ru; Tel.: +7-7052867747

Abstract

In this paper, the dynamic modeling of the anisotropic non-ideal gyroscopic rotor system is considered. The equations of nonstationary transitions are derived from the motion differential equations, from there the control equation and stationary frequency dependencies, force and energy relations. When the rigidity of the elastic support is anisotropic in orthogonal directions, two critical velocities and, accordingly, two resonance regions are found. Because of the strong interaction of the rotor system with a non-ideal DC motor, slopes of the resonance curves are observed in the regions of critical speeds even in the absence of a non-linear component of the reference stiffness, and loops. It has been proven that the cubic nonlinearity of damping strongly suppresses the resonant amplitudes of the rotor, reduces the size of the loops even more, and strongly attenuates the Sommerfeld effects until they are completely eliminated than linear damping. It is shown that an increase in the magnitude of the cubic nonlinearity of damping greatly facilitates the passage of the resonance region and expands the range of operating speeds. This proves that the amplification of linear damping with cubic nonlinearity of damping is one of the methods for controlling resonant passages and an effective damping model.

Keywords: gyroscopic rotary system; dynamic modeling; stiffness anisotropy; non-ideal source; Sommerfeld effect; non-linearity of damping

1. Introduction

Any real drive can only deliver a limited amount of power [1]. If the power of the energy source (electric motor) is not enough power to overcome the resonance, the rotor speed can hang in various regions of structural resonance. Continuous operation while the system is in resonance can lead to alarmingly high levels of vibration and damage to the rotor bearings; or, in extreme cases, to a general failure of the system [2–6]. This is known as velocity capture or resonance capture. However, when the power supply is increased to a certain limit, the captured speed almost instantly jumps to a much higher value. The speed jump is also accompanied by a corresponding drop in vibration amplitudes. This "jump" implies a sudden exit from resonance. In the literature, this jump phenomenon with all its manifestations is recognized as the Sommerfeld effect that arises due to the internal energy coupling between the drive and the driven system, and are important design considerations in the development of various rotating machines with flexible supports (bearings) [2–4,7]. An extended overview on the appearance of the Sommerfeld effect and saturation phenomenon in non-ideal vibrating systems (NIS) in macro and MEMS scales is given in [8].

As a result of analyzing the dynamics of rotor systems supported by fluid film bearings (idealized as anisotropic flexible bearings), it was found that, assuming rigid bearings for such systems, it can lead to a huge inaccuracy in the calculations of critical speeds [9]. On the other hand, some other notable work has shown that the use of flexible supports (instead of rigid supports) can actually improve the stability characteristics of rotor systems [10–13].

It is known that most industrial rotor systems operate in the supercritical speed ranges. To control systems at such high speeds, it is necessary to smoothly pass through the resonance zone.

 doi:10.20944/preprints202605.1561.v1

This is where the consideration of non-ideal drive dynamics and their mutual interaction with the dynamics of the rotor system becomes a matter of concern.

In [14,15], due to anisotropic supports, the Sommerfeld effect is observed at the first critical forward rotation speed and the first critical backward rotation speed. When these critical speeds are far apart, the Sommerfeld effect at the critical backward rotation speed is less pronounced than at the critical forward speed. However, when these critical velocities are close to each other, the severity of the Sommerfeld effects on each of them becomes comparable. In addition, exiting a resonance at a lower critical rate may lead to entrapment in another resonance at a higher critical rate.

In [16], the influence of external damping, eccentricity, fiber tilt angle, nonlinearity and coupling on the occurrence of the Sommerfeld phenomenon and the rotor response was investigated in the unsteady dynamics of a composite shaft.

The rotor system on a shaft with asymmetric bending flexibility supported on bearings has many stable and unstable speed ranges [17]. In certain situations, exiting one unstable speed range may result in capture in another unstable speed range, or simultaneous exit from the next unstable range (the Sommerfeld effect of the second kind).

Sommerfeld effects are being investigated to avoid resonant capture. So, the attenuation of such an effect is extremely important for a smooth resonant transition and stable operation of the rotors at high speeds. In the article [18], in an unbalanced flexible shaft-disk system, as the displacement current of linearized active magnetic bearings (AMB) gradually increases, the amplitude of the turbulence decreases, in turn, the Sommerfeld effect weakens, at a certain value of the displacement current, it will completely cease to exist.

Recently, there has been a growing interest in non-linear approaches in the design of vibration isolation systems. Papers [19–22] confirm that the cubic nonlinearity of damping can not only suppress response at resonance, but also improve isolation at high frequencies (velocities) and can significantly reduce the Sommerfeld effect with the non-linear jump until it is completely eliminated.

If we take into account that the resonant transitions of a rotor with a non-ideal motor through critical speeds with anisotropy of the rigidity of the elastic support are accompanied by resonant captures and jumping effects with two Sommerfeld effects, then the study of the characteristics of these effects and methods for their weakening and further complete elimination, including by the method of using the cubic nonlinearity of damping are especially relevant from scientific and practical points of view.

2. Materials and Methods

2.1. Equations of Motion

A non-ideal system gyroscopic rotor–DC motor is considered (Figure 1). The rotor consists of a disk, a shaft and a support device. The disk has mass m, moment of inertia about its polar axis J_P, moment of inertia about its diametrical axis J_D, and is fixed without skewness at the free end of the rigid shaft. The shaft without mass with length l_1, is installed vertically with the help of the lower hinged and the upper elastic support spaced from it at a distance l_2. With such a location of the disk on the shaft relative to the supports and at a sufficiently high speed of rotation of the shaft $\dot{\varphi}$, the system can be considered as a gyroscopic rotor. In a fixed coordinate system $Oxyz$ the position of the geometric center of the disk S determines the coordinates x, y, z, and the spatial position of the shaft determines the angles α, β and an angle of rotation φ. We will take the coordinate z equal to $z = l_1 = \text{const}$ and exclude it from. consideration. Next, we denote the coordinates of the center of masses m of the disk through x_m and y_m. We also assume that the linear eccentricity e_r is directed along the N axis of the $ONKZ$ coordinate system. In the case of small deviations of the rotor axis $\sin\alpha \approx \alpha, \sin\beta \approx \beta, \cos\alpha \approx 1, \cos\beta \approx 1$.

 doi:10.20944/preprints202605.1561.v1

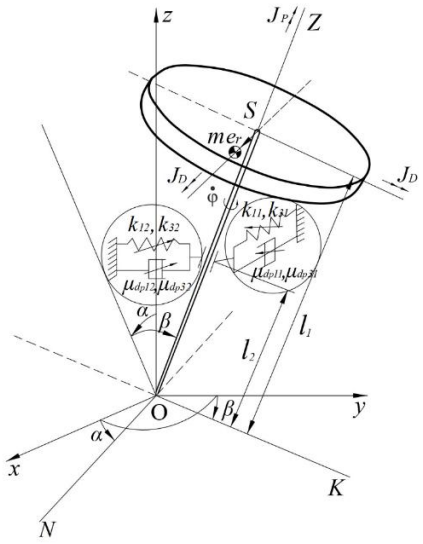

Figure 1. Rotor geometry.

Considering the foregoing, the projections of the angular velocity on the coordinate axes of the *ONKZ* system can be written as

$$\omega_N \approx -\dot{\beta}, \omega_K \approx \dot{\alpha}, \omega_Z \approx \dot{\varphi} + \dot{\alpha} \cdot \beta + \alpha \cdot \dot{\beta}. \tag{1}$$

Relationship between coordinates x and x_m, y and y_m is expressed by the following relations:

$$\begin{aligned} x_m &= x + e_r \cos\varphi = l_1\alpha + e_r \cos\varphi, \\ y_m &= y + e_r \sin\varphi = l_1\beta + e_r \sin\varphi. \end{aligned} \tag{2}$$

Thus, the position of the rigid shaft and the rotor as a whole in space is determined by the angles α, β and φ.

It is convenient to represent the equations of motion of the rotor in the form of the Lagrange equations of the second kind. To do this, we first compose an expression for the kinetic energy of the disk in accordance with Koenig's theorem [23]:

$$T = \frac{1}{2}m\left(\dot{x}_m^2 + \dot{y}_m^2\right) + \frac{1}{2}\left(J_K\omega_K^2 + J_N\omega_N^2 + J_Z\omega_Z^2\right).$$

Assuming that $J_K = J_N = J_D, J_Z = J_P$ as and using (1) and the relationship (2) between the coordinates x and x_m, y and y_m the expression for the kinetic energy of the rotor is presented in the final form

$$T = \frac{1}{2}m\left[\left(l_1\dot{\alpha} - e_r\sin\varphi\dot{\varphi}\right)^2 + \left(l_1\dot{\beta} + e_r\cos\varphi\dot{\varphi}\right)^2\right] + \frac{1}{2}J_D\left(\dot{\beta}^2 + \dot{\alpha}^2\right) + \frac{1}{2}J_P\left(\dot{\varphi} + \dot{\alpha}\cdot\beta + \alpha\cdot\dot{\beta}\right)^2. \tag{3}$$

The projections of the moment of gravitational force have the form:

$$M_K = \left(l_1\alpha + e_r\cos\varphi\right)G, M_N = \left(l_1\beta + e_r\sin\varphi\right)G, \tag{4}$$

where $G = mg$ – disk weight.

As is known, the resonant properties of nonlinear oscillatory systems depend very much on the properties of the energy source, on its characteristics [1]. In [24,25] it was assumed that the torque of an engine used in a nonideal oscillatory system is proportional to the rotational speed of its shaft.

The dynamic moment of the motor in accordance with [1,26] has the following expression in general form:

 doi:10.20944/preprints202605.1561.v1

$$M_{dm}(\dot{\varphi}) = M_{mt}(\dot{\varphi}) - q_{rm}\dot{\varphi}, \tag{5}$$

where $M_{mt}(\dot{\varphi})$ is the motor torque (motor characteristic), $q_{rm}\dot{\varphi}$ is the moment of resistance force to the rotation of the motor rotor.

In [27], the possibility and expediency of using static characteristics of energy sources in the equations of motion, as well as the acceptability of restrictions and assumptions used in the analysis of the equations of motion, were experimentally confirmed. Then, in accordance with [28,29], substituting the found value M_{mt} into (5), we obtain an expression for the dynamic moment of an electric motor with a permanent magnet in the form:

$$M_{dm} = \frac{c_M \Phi_m}{R} U - \left(\frac{c_M c_E \Phi_m^2}{R} + q_{rm} \right) \dot{\varphi}, \tag{6}$$

where Φ_m - the magnetic flux of one pole, $\dot{\varphi}$ - the angular velocity of rotation of the armature, U - the voltage applied to the electrical circuit of the motor, R - the resistance of the entire power circuit, the electrical constant c_E and mechanical constant c_M are equal to each other, q_m - the coefficient of resistance to rotation of the motor rotor.

The upper bearing support of the gyroscopic rotor can be made of non-linear viscoelastic materials such as caoutchouc, rubber and other polymers widely used as vibration dampers. As is known, rubber shock absorbers, in addition to linear viscoelastic properties, have both nonlinearity of damping and nonlinear stiffness [30,31].

There are various non-linear damping models. The phenomenological model of nonlinear damping is added to the equations of motion of studies [19–23,31,33–35] and other studies. It considers two types of n-th damping terms: the first type is represented by the velocity multiplied by the (n–1)-th power of the displacement, and the second type is proportional to the n-th degree of velocity [19–23,30,35]. The mechanism of nonlinearity of damping was modeled by the scattering of thermally excited vibrational modes from the assumed eigenmode in [36].

In accordance with the second damping type, the moments of the dissipative forces with linear and cubic nonlinear components acting in the flexible support can be described by the Rayleigh function, in its more general form:

$$\Phi = \frac{1}{2}\left(\mu_{dp11}\dot{\alpha}^2 + \mu_{dp12}\dot{\beta}^2\right) + \frac{1}{4}\left(\mu_{dp31}\dot{\alpha}^4 + \mu_{dp32}\dot{\beta}^4\right), \tag{7}$$

where μ_{dp11}, μ_{dp12} - coefficients of linear viscous damping and μ_{dp31}, μ_{dp32} - coefficients of cubic nonlinearity of damping in mutually perpendicular directions. The coefficients of linear damping and cubic nonlinearity of damping have different dimensions and may differ in values.

The studies carried out in [37,38] are very attractive. Experiments show a strong increase in damping with oscillation amplitude for non-linear oscillations of beams, plates and shells. Non-linear damping is determined in research by viscoelasticity using a single degree of freedom model derived from a standard linear solid material that includes geometric non-linearity. The developed damping model is represented by the product of the velocity by the square of the displacement, and its parameters are determined experimentally. The results of the study of forced vibration responses measured for a rectangular plate with a free edge are interesting in that it is a case where energy does not pass through the boundary.

If we take into account that the rotor shaft is rigid, and only its upper support has anisotropic elasticity, and the elastic forces in mutually perpendicular coordinate directions are respectively equal to $F_x = k_{11}x_2 + k_{31}x_2^3 = k_{11}l_2\alpha + k_{31}l_2^3\alpha^3$, $F_y = k_{12}y_2 + k_{32}y_2^3 = k_{12}l_2\beta + k_{32}l_2^3\beta^3$, then the potential energy of the system can be represented as

 doi:10.20944/preprints202605.1561.v1

$$V = \frac{1}{2} l_2^2 \left(k_{11} \alpha^2 + k_{12} \beta^2 \right) + \frac{1}{4} l_2^4 \left(k_{31} \alpha^4 + k_{32} \beta^4 \right), \quad (8)$$

where k_{11}, k_{12} - coefficients of linear rigidity and k_{31}, k_{32} – coefficients of non-linear rigidity of the support in mutually perpendicular directions.

We represent the Lagrange equations of the second kind for the rotor system as follows:

$$\frac{d}{dt}\left(\frac{\partial T}{\partial \dot{q}_i} \right) - \frac{\partial T}{\partial q_i} + \frac{\partial V}{\partial q_i} = -\frac{\partial \Phi}{\partial \dot{q}_i} + Q_i, (i = 1, 2, 3). \quad (9)$$

Here generalized coordinates $q_i : q_1, q_2, q_3$ are represented by angular coordinates α, β, φ, generalized forces $Q_i : Q_1, Q_2, Q_3$ - by projections of the moment of gravity M_K, M_N and dynamic torque of the motor M_{dm}, defined by formulas (4) and (6).

Substituting expressions (3), (4), (6) – (8) into (9), and discarding the perturbations containing $\ddot{\varphi}$, since in the region close to the resonant velocity $\ddot{\varphi} << \dot{\varphi}^2$, and perturbations having the parameter J_P, since in what follows we assume that $J_P << J_D$, and quantities of the second and higher orders of smallness with respect to the angular coordinates α and β, and their derivatives, and their combinations, we obtain the equations of motion of the rotor

$$\begin{aligned}
&\left(J_D + m l_1^2 \right) \ddot{\alpha} + J_P \dot{\varphi} \dot{\beta} + \mu_{dp11} \dot{\alpha} + \mu_{dp31} \dot{\alpha}^3 + \left(k_{11} l_2^2 - m g l_1 \right) \alpha + k_{31} l_2^4 \alpha^3 = m e_r \dot{\varphi}^2 l_1 \cos\varphi, \\
&\left(J_D + m l_1^2 \right) \ddot{\beta} - J_P \dot{\varphi} \dot{\alpha} + \mu_{dp12} \dot{\beta} + \mu_{dp32} \dot{\beta}^3 + \left(k_{12} l_2^2 - m g l_1 \right) \beta + k_{32} l_2^4 \beta^3 = m e_r \dot{\varphi}^2 l_1 \sin\varphi, \quad (10) \\
&J_P \ddot{\varphi} = m e_r l_1 \left(\ddot{\alpha} \sin\varphi - \ddot{\beta} \cos\varphi \right) - J_P \left(\ddot{\alpha}\beta + 2\dot{\alpha}\dot{\beta} + \alpha\ddot{\beta} \right) + c_M \Phi_m U / R - \left(c_M c_E \Phi_m^2 / R + q_m \right) \dot{\varphi}.
\end{aligned}$$

In the right part of the obtained system of equations (10), the components of the projections of the moment of gravity were also neglected, since $m e_r \dot{\varphi}^2 l_1 >> m g e_r$ for a fast-rotating rotor.

Natural frequencies (critical speeds) of a dampened rotor system (10):

$$\omega_{1,2} = \sqrt{b/2 \mp \sqrt{b^2/4 - c}}, \quad (11)$$

where

$$b = \frac{\left(J_D + m l_1^2 \right) \left[\left(k_{11} l_2^2 - m g l_1 \right) + \left(k_{12} l_2^2 - m g l_1 \right) \right]}{\left(J_D + m l_1^2 \right)^2 - J_P^2}, c = \frac{\left(k_{11} l_2^2 - m g l_1 \right) \left(k_{12} l_2^2 - m g l_1 \right)}{\left(J_D + m l_1^2 \right)^2 - J_P^2}, \quad (12)$$

in case $J_D >> J_P$: $b = \left(k_{11} l_2^2 - m g l_1 \right) / \left(J_D + m l_1^2 \right) + \left(k_{12} l_2^2 - m g l_1 \right) / \left(J_D + m l_2^2 \right)$, $c = \left[\left(k_{11} l_2^2 - m g l_1 \right) / \left(J_D + m l_1^2 \right) \right] \left[\left(k_{12} l_2^2 - m g l_1 \right) / \left(J_D + m l_1^2 \right) \right]$.

For numerical calculations using formulas (11) and (12), some geometric and dynamic parameters of the gyroscopic rotor system are borrowed from the experimental setup used in [20,39]: l_1 = 0.46 m, l_2 = 0.33 m, m = 2 kg, k_{11} = 2 104 Nm^{-1}, k_{12} = 2.4 104 Nm^{-1}, J_D = 0.090 kgm^2, J_P = 0.011 kgm^2, e_r = 0.0193 m.

Now we can calculate the natural frequencies (critical speeds) of the gyroscopic rotor system (10): ω_1 = 64.94 Hz, ω_2 = 71.34 Hz.

Own angular velocity of rotation of the shaft ω_1 in the interval [64.95 Hz, 64.48 Hz] can be approximately considered constant and equal to ω_1 = 65 Hz. This makes it possible to use ω_1 in the process of bringing the parameters $t, \omega, G, k_{11}, k_{12}, k_{31}, k_{32}, \mu_{dp11}, \mu_{dp12}, \mu_{dp31}, \mu_{dp32}$ into a dimensionless form.

We introduce the following dimensionless parameters:

 doi:10.20944/preprints202605.1561.v1

$$
\begin{gathered}
l = l_2/l_1;\bar{t} = t\omega_1;\varphi' = \dot{\varphi}/\omega_1;\bar{J}_P = J_P/(ml_1^2);\bar{J}_D = J_D/(ml_1^2);\bar{G} = g/\left(l_1\omega_1^2\right);\\
K_{11} = k_{11}/\left(m\omega_1^2\right);K_{12} = k_{12}/\left(m\omega_1^2\right);e = e_r/\left[l_1\left(1+\bar{J}_D\right)\right];K_{31} = k_{31}l_2^4/\left[ml_1^2\omega_1^2\left(1+\bar{J}_D\right)\right];\\
K_{32} = k_{32}l_2^4/\left[ml_1^2\omega_1^2\left(1+\bar{J}_D\right)\right];\mu_{11} = \mu_{dp11}/\left[ml_1^2\omega_1^2\left(1+\bar{J}_D\right)\right];\mu_{12} = \mu_{dp12}/\left[ml_1^2\omega_1^2\left(1+\bar{J}_D\right)\right];\\
\mu_{31} = \mu_{dp31}\omega_1/\left[ml_1^2\left(1+\bar{J}_D\right)\right];\mu_{32} = \mu_{dp32}\omega_1/\left[ml_1^2\left(1+\bar{J}_D\right)\right];J_{P1} = \bar{J}_P/\left(1+\bar{J}_D\right);\\
u_1 = c_M\Phi_m U/\left[Rml_1^2\left(1+\bar{J}_D\right)\omega_1^2\right];u_2 = \left(c_M c_E\Phi_m^2/R+q_{rm}\right)/\left[ml_1^2\omega_1\left(1+\bar{J}_D\right)\right].
\end{gathered}
\tag{13}
$$

With the use of (13), the equations of motion (10) can be represented in a dimensionless form:

$$
\begin{gathered}
\alpha'' + J_{P1}\varphi'\beta' + \mu_{11}\alpha' + \mu_{31}\alpha'^3 + \omega_{n1}^2\alpha + K_{31}\alpha^3 = e\varphi'^2\cos\varphi,\\
\beta'' - J_{P1}\varphi'\alpha' + \mu_{12}\beta' + \mu_{32}\beta'^3 + \omega_{n2}^2\beta + K_{32}\beta^3 = e\varphi'^2\sin\varphi,\\
\varphi'' = \left[e\left(\alpha''\sin\varphi - \beta''\cos\varphi\right) - J_{P1}\left(\alpha''\beta + 2\alpha'\beta' + \alpha\beta''\right) + u_1 - u_2\varphi'\right]/J_P,
\end{gathered}
\tag{14}
$$

where

$$
\omega_{n1} = \sqrt{\left(K_{11}l^2 - \bar{G}\right)/\left(1+\bar{J}_D\right)} \tag{15}
$$

– is the dimensionless natural frequency of the rotor system (14) at $K_1 = K_{11}$,

$$
\omega_{n2} = \sqrt{\left(K_{12}l^2 - \bar{G}\right)/\left(1+\bar{J}_D\right)} \tag{16}
$$

– is the dimensionless natural frequency of the rotor system (14) at $K_1 = K_{12}$, where $\bar{J}_D$ >> $\bar{J}_P$. is accepted.

In the third equation of system (14)

$$
u_1 - u_2\varphi' = M \tag{17}
$$

- is the dimensionless dynamic torque of the motor. Here u_1 is the dimensionless normalized motor voltage, (control parameter), which depends on the voltage on the motor; u_2 is a parameter depending on the type of energy source [14,29].

Here, the prime denotes the derivative with respect to the dimensionless time $\bar{t}$.

We are interested in the effect of cubic nonlinearity of damping on the dynamics of a weakly nonlinear rotor system, taking into account the anisotropy of the support rigidity and the change in voltage on the motor with a characteristic taken as a straight line [14,29].

To use the Bogolyubov method [1,20,40–42], the following restrictions are accepted for the analytical solution of the equations of motion. The projections of the moments of linear and nonlinear damping forces $\mu_{11}\alpha', \mu_{12}\beta'$ and $\mu_{31}\alpha'^3, \mu_{32}\beta'^3$, as well as the moment of the nonlinear elastic force $K_{31}\alpha^3, K_{32}\beta^3$, moments of inertia forces $e\varphi'^2\cos\varphi, e\varphi'^2\sin\varphi,\ e\alpha''\sin\varphi, -e\beta''\cos\varphi$ and passive gyroscopic moments $-J_{P1}\Omega\alpha', J_{P1}\Omega\beta', -J_{P1}\left(\alpha''\beta + 2\alpha'\beta' + \alpha\beta''\right)$ are assumed to be small compared to other moments of forces acting in the system. Due to the fact that we confine ourselves to considering regimes close to stationary motions, the acceleration φ'' will be small. We will also confine ourselves to considering motion in resonance regions, where the frequencies of free oscillations ω_{n1}, ω_{n2} are close to the frequency of forced oscillations Ξ, i.e. the values of the so-called frequency detuning $\Delta_1 = \omega_{n1} - \Xi, \Delta_2 = \omega_{n2} - \Xi$ are small. In order to reflect the smallness of the upsets Δ_1 and Δ_2 in an explicit form, we will further represent them using a dimensionless small positive parameter ε in the form of the relations $\Delta_1 = \varepsilon\tilde{\sigma}_1$, $\Delta_2 = \varepsilon\tilde{\sigma}_2$, where $\tilde{\sigma}_1$ and $\tilde{\sigma}_2$ have the same dimension as Δ_1 or Δ_2.

Equations (14), after the introduction of a small parameter in accordance with the accepted constraints of the problem and the new notation for values

 doi:10.20944/preprints202605.1561.v1

$$\begin{aligned}&\mu_{11}=\varepsilon\tilde{\mu}_{11},\mu_{12}=\varepsilon\tilde{\mu}_{12},\mu_{31}=\varepsilon\tilde{\mu}_{31},\mu_{32}=\varepsilon\tilde{\mu}_{32},K_{31}=\varepsilon\tilde{K}_{31},\\&K_{32}=\varepsilon\tilde{K}_{32},J_{P1}=\varepsilon\tilde{J}_{P},e=\varepsilon\tilde{e},u_1=\varepsilon\tilde{u}_1,u_2=\varepsilon\tilde{u}_2\end{aligned}\tag{18}$$

will look as follows:

$$\begin{aligned}&\alpha''+\omega_{n1}^2\alpha=\varepsilon\left(\tilde{e}\varphi'^2\cos\varphi-\tilde{J}_P\varphi'\beta'-\tilde{\mu}_{11}\alpha'-\tilde{\mu}_{31}\alpha'^3-\tilde{K}_{31}\alpha^3\right),\\&\beta''+\omega_{n2}^2\beta=\varepsilon\left(\tilde{e}\varphi'^2\sin\varphi+\tilde{J}_P\varphi'\alpha'-\tilde{\mu}_{12}\beta'-\tilde{\mu}_{32}\beta'^3-\tilde{K}_{32}\beta^3\right),\\&\varphi''=\varepsilon\left[\tilde{e}\left(\alpha''\sin\varphi-\beta''\cos\varphi\right)-\tilde{J}_P\left(\alpha''\beta+2\alpha'\beta'+\alpha\beta''\right)+\tilde{u}_1-\tilde{u}_2\varphi'\right]\Big/J_{P1}.\end{aligned}\tag{19}$$

Equations (19) are a system of non-linear ordinary differential equations of the second order with respect to α,β and φ with a small parameter ε for a non-ideal anisotropic gyroscopic rotor system.

2.2. Solutions of Equations of Motion

At small angular deviations of the shaft α and β, harmonic oscillations at the frequency of the driving moment predominate in the solutions of system (19). Due to the anisotropy of the support rigidity in orthogonal directions, oscillations in these directions occur in different ways: with different amplitudes and different phases. Then we define the solutions of system (19) in the following form

$$\alpha=A\cos\left(\varphi+\xi\right),\tag{20}$$

$$\beta=B\sin\left(\varphi+\zeta\right).\tag{21}$$

Here A,B are the oscillation amplitudes in mutually perpendicular directions, ξ,ζ are the phase shift angles between the angular coordinates α, β and the disturbing moment, respectively. They represent the most essential parameters of motion and are slowly varying functions of time $\bar{t}$.

Following the method of Bogolyubov's theory of small perturbations [1,20,40–42], taking into account (20) and (21), we obtain a system of vorticity equations equivalent to the system (14), approximate solutions of which can be found in the form

$$\begin{aligned}&\Xi=\Omega+\varepsilon U_1\left(\bar{t},\Omega,a,b,\gamma,\delta\right),\\&A=a+\varepsilon U_2\left(\bar{t},\Omega,a,b,\gamma,\delta\right),\gamma=\xi+\varepsilon U_3\left(\bar{t},\Omega,a,b,\gamma,\delta\right),\\&B=b+\varepsilon U_4\left(\bar{t},\Omega,a,b,\gamma,\delta\right),\delta=\zeta+\varepsilon U_5\left(\bar{t},\Omega,a,b,\gamma,\delta\right),\end{aligned}\tag{22}$$

where $\varepsilon U_1\left(\bar{t},\Omega,a,b,\gamma,\delta\right),\varepsilon U_2\left(\bar{t},\Omega,a,b,\gamma,\delta\right),\varepsilon U_3\left(\bar{t},\Omega,a,b,\gamma,\delta\right),\varepsilon U_4\left(\bar{t},\Omega,a,b,\gamma,\delta\right),\varepsilon U_5\left(\bar{t},\Omega,a,b,\gamma,\delta\right)$ are small periodic functions of time $\bar{t}$.

After averaging and excluding a small parameter ε in accordance with the formulas for converting parameter values (18), the equations for nonstationary vorticity follow from the obtained averaged equations of the first approximation [20,31] with respect to the oscillatory parameters a,b,γ,δ,Ω of the first harmonic, depending on the dimensionless motor voltage u_1:

 doi:10.20944/preprints202605.1561.v1

$$\begin{aligned}
\frac{d\Omega}{d\bar{t}} &= \frac{1}{J_{P1}}\left[\begin{array}{l} u_1 - u_2\Omega + \frac{1}{2}e\Omega\left(a\omega_{n1}\sin\gamma + b\omega_{n2}\sin\delta\right) + \\ \frac{1}{2}J_{P1}ab\left[2\omega_{n1}\omega_{n2} - \Omega\left(\omega_{n1}+\omega_{n2}\right)\right]\sin\left(\gamma-\delta\right)\end{array}\right], \\
\frac{da}{d\bar{t}} &= -\frac{1}{2\omega_{n1}}\left[e\Omega^2\sin\gamma - J_{P1}\Omega b\omega_{n2}\sin\left(\gamma-\delta\right) + \mu_{11}\omega_{n1}a + \frac{3}{4}\mu_{31}\left(\omega_{n1}a\right)^3\right], \\
\frac{d\gamma}{d\bar{t}} &= \omega_{n1} - \Omega - \frac{1}{2\omega_{n1}a}\left[e\Omega^2\cos\gamma - J_{P1}\Omega b\omega_{n2}\cos\left(\gamma-\delta\right) - \frac{3}{4}K_{31}a^3\right], \\
\frac{db}{d\bar{t}} &= -\frac{1}{2\omega_{n2}}\left[e\Omega^2\sin\delta + J_{P1}\Omega a\omega_{n1}\sin\left(\gamma-\delta\right) + \mu_{12}\omega_{n2}b + \frac{3}{4}\mu_{32}\left(\omega_{n2}b\right)^3\right], \\
\frac{d\delta}{d\bar{t}} &= \omega_{n2} - \Omega - \frac{1}{2\omega_{n2}b}\left[e\Omega^2\cos\delta - J_{P1}\Omega a\omega_{n1}\cos\left(\gamma-\delta\right) - \frac{3}{4}K_{32}b^3\right], \\
\frac{d\varphi}{d\bar{t}} &= \Omega.
\end{aligned} \tag{23}$$

Under the conditions of the existence of stationary modes of motion,

$$d\Omega/d\bar{t} = 0, da/d\bar{t} = 0, db/d\bar{t} = 0, d\gamma/d\bar{t} = 0, d\delta/d\bar{t} = 0$$

we obtain from (23) the control equation (frequency equation) and the equations of stationary joint amplitude- and phase-frequency characteristics:

$$\begin{array}{l} u_1 - u_2\Omega + 0.5e\Omega\left(a\omega_{n1}\sin\gamma + b\omega_{n2}\sin\delta\right) + \\ 0.5J_{P1}ab\left[2\omega_{n1}\omega_{n2} - \Omega\left(\omega_{n1}+\omega_{n2}\right)\right]\sin\left(\gamma-\delta\right) = 0, \end{array} \tag{24}$$

$$\begin{aligned}
&e\Omega^2\sin\gamma - J_{P1}\Omega b\omega_{n2}\sin\left(\gamma-\delta\right) + \mu_{11}\omega_{n1}a + \frac{3}{4}\mu_{31}\left(\omega_{n1}a\right)^3 = 0, \\
&\omega_{n1} - \Omega - \frac{1}{2\omega_{n1}a}\left[e\Omega^2\cos\gamma - J_{P1}\Omega b\omega_{n2}\cos\left(\gamma-\delta\right) - \frac{3}{4}K_{31}a^3\right] = 0, \\
&e_r\Omega^2\sin\delta + J_{P1}\Omega a\omega_{n1}\sin\left(\gamma-\delta\right) + \mu_{12}\omega_{n2}b + \frac{3}{4}\mu_{32}\left(\omega_{n2}b\right)^3 = 0, \\
&\omega_{n2} - \Omega - \frac{1}{2\omega_{n2}b}\left[e\Omega^2\cos\delta - J_{P1}\Omega a\omega_{n1}\cos\left(\gamma-\delta\right) - \frac{3}{4}K_{32}b^3\right] = 0.
\end{aligned} \tag{25}$$

From (24), the first, and third equations of system (25), and assuming that relations $\omega_n/\Omega \approx 1$ and $\omega_n \approx \Omega$ are possible in the resonance region, we obtain the so-called control equation [29,30] in the following form:

$$u_1 - u_2\Omega - \frac{1}{2}\left(\mu_{11}\omega_{n1}a^2 + \mu_{12}\omega_{n2}b^2\right) - \frac{3}{8}\left(\mu_{31}\omega_{n1}^3a^4 + \mu_{32}\omega_{n2}^3b^4\right) = 0. \tag{26}$$

Having jointly solved the equations of system (25) numerically, we find the amplitudes a and b, initial phases γ and δ, and stationary oscillations. Equations (25) and (26), when the conditions $\omega_{n1} = \omega_{n2} = \omega_n$, $\mu_{11} = \mu_{12} = \mu_1$, $\mu_{31} = \mu_{32} = \mu_3$, $a=b$ are satisfied, are converted into expressions for the case of a rotor with an elastic support with isotropic reducing and damping properties [20,30].

The dependence of the oscillation frequency Ξ on time $\bar{t}$, taking into account the higher harmonics, is defined as

$$\begin{array}{l} \Xi = \Omega + \left[e/\left(4J_{P1}\right)\right]\left[\omega_{n1}a\cos\left(2\varphi+\gamma\right) - \omega_{n2}b\cos\left(2\varphi+\delta\right)\right] - \\ \left[ab/\left(4\Omega\right)\right]\left[2\omega_{n1}\omega_{n2} - \Omega\left(\omega_{n1}+\omega_{n2}\right)\right]\cos\left(2\varphi+\gamma+\delta\right). \end{array} \tag{27}$$

 doi:10.20944/preprints202605.1561.v1

The results of the research show that the higher harmonics of the oscillations practically do not affect the amplitudes, phases (22) and oscillograms of the deviation angles α and β, their oscillations are practically harmonic [20].

2.3. Ratio of Moments, and Ratios of Power and Energy

In the case of a non-ideal rotor system, the parameter u_1 should be determined as the roots of equation (26), which will correspond to the values of the amplitudes a and b, phases γ and δ, and oscillations in orthogonal directions, calculated according to (25). If we take into account that the characteristic of the motor is pre-selected as a straight line, then the corresponding required dynamic moment of the motor is:

$$M = u_1 - u_2\Omega. \tag{28}$$

Eq. (26) can be assumed as an equilibrium equation for the moment of the moving forces of the energy source and the moments of vibration damping forces in the steady state. From (26), by multiplication term by term by Ω, one can obtain the power equation:

$$(u_1 - u_2\Omega)\Omega - \frac{1}{2}\Omega\left(\mu_{11}\omega_{n1}a^2 + \mu_{12}\omega_{n2}b^2\right) - \frac{3}{8}\Omega\left(\mu_{31}\omega_{n1}^3a^4 + \mu_{32}\omega_{n2}^3b^4\right) = 0, \tag{29}$$

where

$$N_m = (u_1 - u_2\Omega)\Omega \tag{30}$$

- dynamic power of the energy source - DC motor;

$$N_d = \frac{1}{2}\Omega\left(\mu_{11}\omega_{n1}a^2 + \mu_{12}\omega_{n2}b^2\right) + \frac{3}{8}\Omega\left(\mu_{31}\omega_{n1}^3a^4 + \mu_{32}\omega_{n2}^3b^4\right) \tag{31}$$

- the power expended on damping the oscillatory motion.

Expression of moments (26), as an expression of powers (28), is easy to obtain from the first integrals of the equations of motion (26) according to the method described in [1,20].

3. Results and their Analysis

3.1. Impact of Damping on Rotor Dynamics

The following values of dimensionless parameters were used for calculation operations: $\omega_{n1} = 1$, $\omega_{n2} = 1.1$, $e = 0.0346$; $J_{p1} = 0.021$; $u_2 = 1.245$. The results of numerical calculations using formulas (25) and (26) are shown in Figures 2–7.

During rotor speedup (speed increase) the steady rotor speed follows the trajectory →a→b→g→c→d→e→, containing frequency capture at lower threshold of stability on the path a→b and on the path c→d, 2 hopping effects b→g and d→e (Figure 2a). During rotor slowdown (speed reduction) the steady rotor speed follows the trajectory →e→f→f→c*→g→h→a*→, containing frequency capture at lower threshold of stability in directions c*→c and a→a*, 2 hopping effects f→c* and h→a* (Figure 2a). In two perpendicular directions the support stiffness has different values and therefore two different jumping effects are observed at two input voltages [42]. The hop sizes in the second critical speed region are comparatively higher than those in the first critical speed region [15]. The resonance zones have an unstable hb branch with a respective hg interval and an unstable fd branch with a respective fe interval of the shaft speed. It should be noted that the speed values along the branches between “b” and “h”, “d” and “f”, which correspond to voltage values of 1.266 to 1.290 and 1.400 to 1.468, respectively, are physically unattainable as due to their instabilities [43–45]. As a result, corresponding to the two stable branches, there are only two possible speed values near the resonance region; one of them can be accessed during speedup operation and the other during slowdown operation.

 doi:10.20944/preprints202605.1561.v1

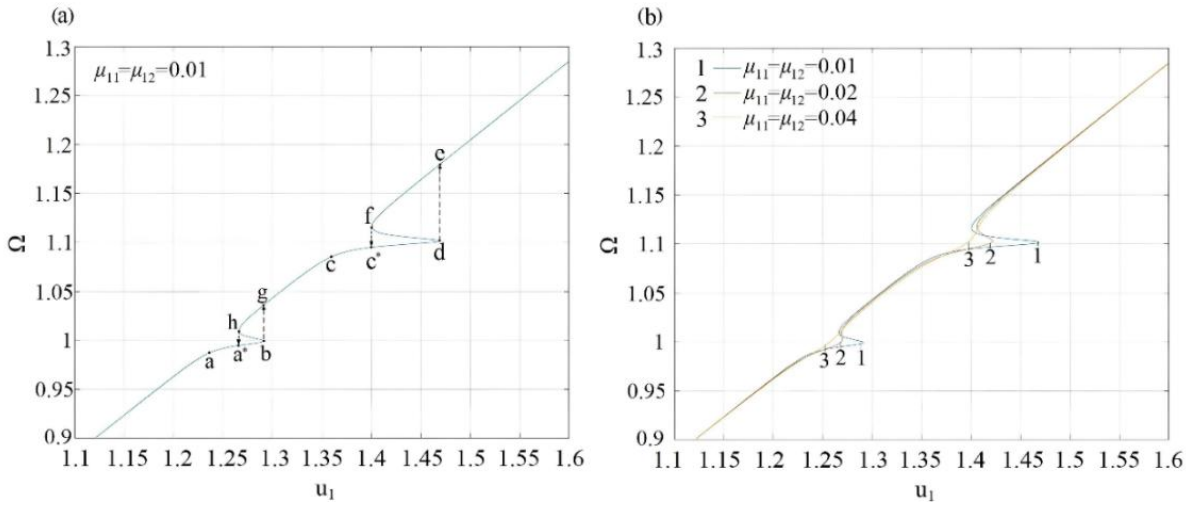

Figure 2. Shaft rotation speed depending on the dimensionless normalized motor voltage at: (a) linear damping coefficient; (b) various values of linear damping coefficient.

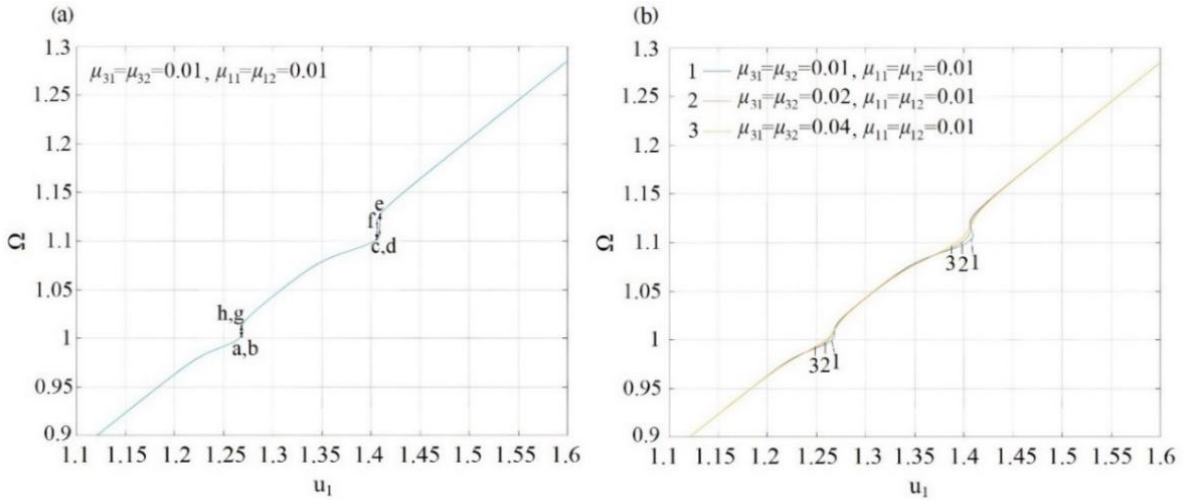

Figure 3. Shaft rotation speed depending on the dimensionless normalized motor voltage at: (a) cubic nonlinearity of damping; (b) various values of cubic nonlinearity of damping.

As the linear damping value increases from 0.01 to 0.02, points b and d shift to the left, points a* and c* shift to the right. Consequently, the size of Ω hops significantly decreases from 1÷1.036 to 1÷1.019 in the first critical speed region, from 1.1÷1.179 to 1.1÷1.141 in the second critical speed region, as well as the size of unstable branches; the Sommerfeld effects are significantly attenuated (Figure 2b) and further increase of linear damping to the value of 0.04 completely removes the above effects (Figure 2b) [3,44].

The addition of a linear damping of magnitude 0.01 with a cubic nonlinearity of damping of magnitude 0.01 (Figure 3a) ensures the disappearance of the unstable branch in the region of the first critical speed, a significant reduction in the size of the jump in Ω from 1.1÷1.179 to 1.1÷1.127, and, consequently, a reduction in the unstable branch in the region of the second critical speed. When the cubic nonlinearity of damping component is further increased to 0.02, (or to 0.04) it virtually removes the Sommerfeld effect in the second resonance region (Figure 3b).

In the structure of the resonant region, as the drive voltage increases and the critical speed approaches, the angular velocity of the shaft does not increase, and the driven energy is spent on excitation of the rotor vibration. When the driven power reaches a critical value, the vibration amplitudes sharply decrease with a simultaneous increase in the speed of rotation of the shaft. Figure 4 are graphs of vibration amplitudes in orthogonal directions versus drive voltage for different values

 doi:10.20944/preprints202605.1561.v1

of linear damping coefficient (Figure 4a) and coefficient of cubic nonlinearity of damping in the presence of a constant value of linear damping $\mu_{11} = \mu_{12} = 0.01$ (Figure 4b), respectively. It is easy to see from them that both values $\mu_{11} = \mu_{12}$ and $\mu_{31} = \mu_{32}$ dampen the maximum resonant amplitudes, but the effect of linear damping combined with cubic nonlinearity of damping.

As the value of linear damping increases $\mu_{11} = \mu_{12}$ from 0.01 to 0.04 (Figure 4a), the dimensions of the loop of the resonance curve for the amplitude a in the second resonant region, for the amplitude b in the first resonant region, decrease. Complementing a linear damping with value of 0.01 with cubic nonlinearity of damping with values 0.01, 0.02 and 0.04 reduces the size of these loops so much that they become the peak points of the amplitude rises (Figure 4b).

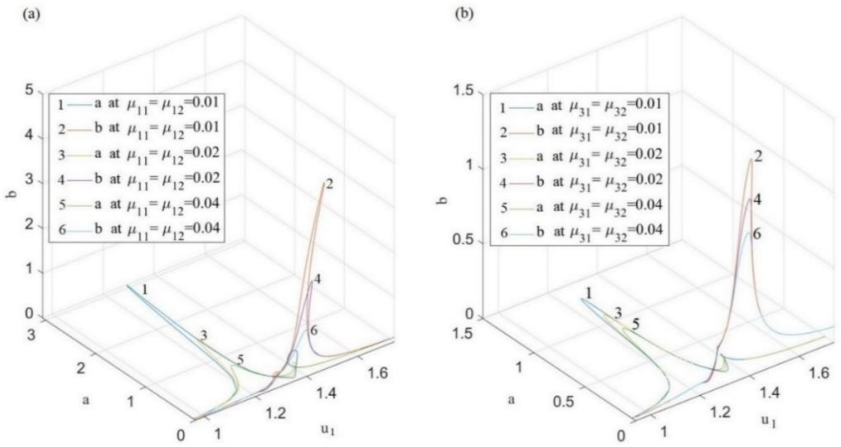

Figure 4. Stationary oscillation amplitudes of an anisotropic rotor depending on the dimensionless normalized supply voltage at various values of the coefficients: (a) linear damping: (b) cubic nonlinearity of damping.

For comparison, Figures 5a and 5b show the stationary amplitude-frequency characteristics of an ideal anisotropic gyroscopic rotor system [45]. In them, instead of the loops observed in the previous figures, there are amplitude elevations, the maximum values of which decrease as the damping value increases. So, due to the strong interaction of the rotor with a non-ideal energy source - a DC motor, the resonance curves of both directions incline towards the drive voltage axis, accompanied by Sommerfeld effects with jumps, and loops appear in them [14].

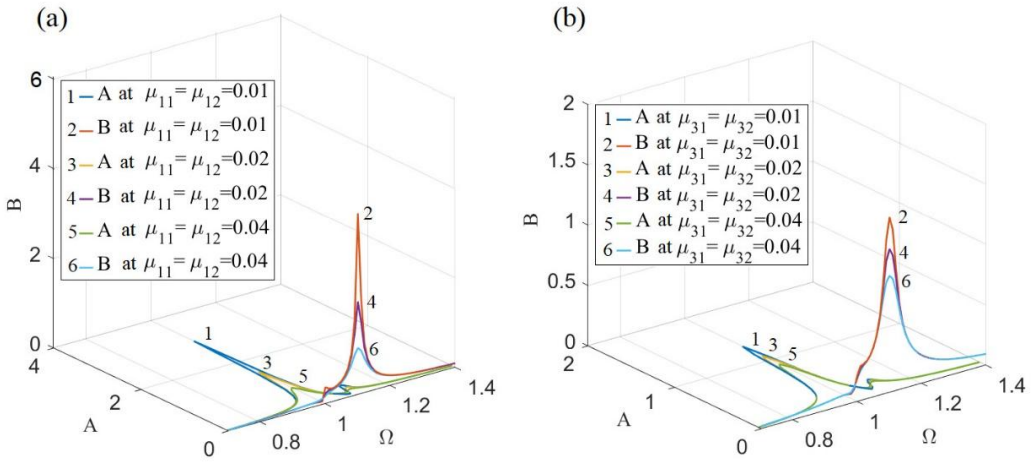

Figure 5. Stationary oscillation amplitudes of a rotor depending on the speed of rotation of the shaft at various values of the coefficients: (a) linear damping; (b) cubic nonlinearity of damping.

 doi:10.20944/preprints202605.1561.v1

Figure 6 show three-dimensional plots between drive voltage, shaft angular velocity, and oscillation amplitude a and b, respectively, for different values of the linear damping coefficients. Under the influence of damping, the hook formed instead of the loop is straightened. However, in a similar graph in Figure 7a there is a loop in the resonance curve formed by the intersection of the amplitude values, which decreases in size as the magnitude of the cubic nonlinearity of damping increases. Branched loop-curves for various values of nonlinearity of damping merge into one line as the voltage and rotation speed.

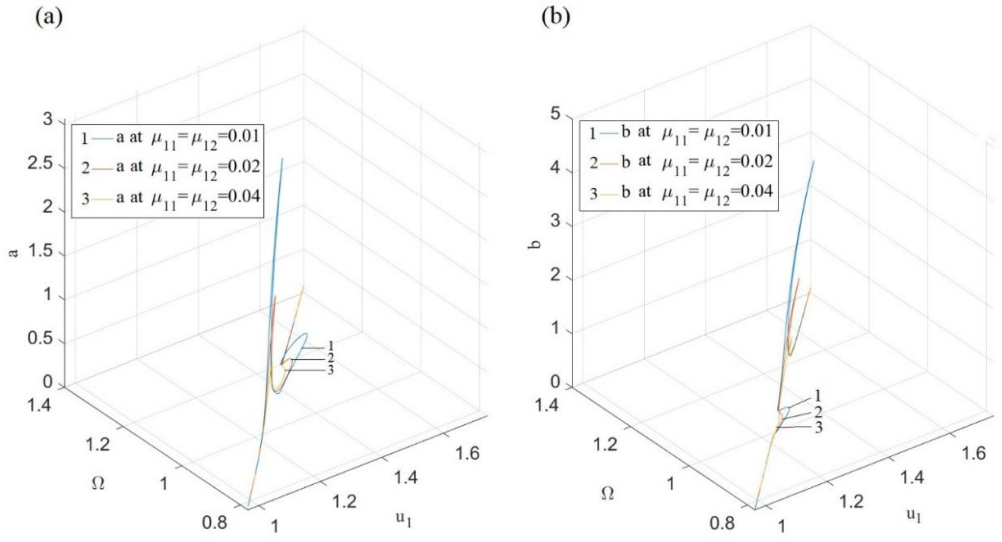

Figure 6. Stationary oscillation amplitudes a (a) and b (b) for various values of the linear damping coefficient.

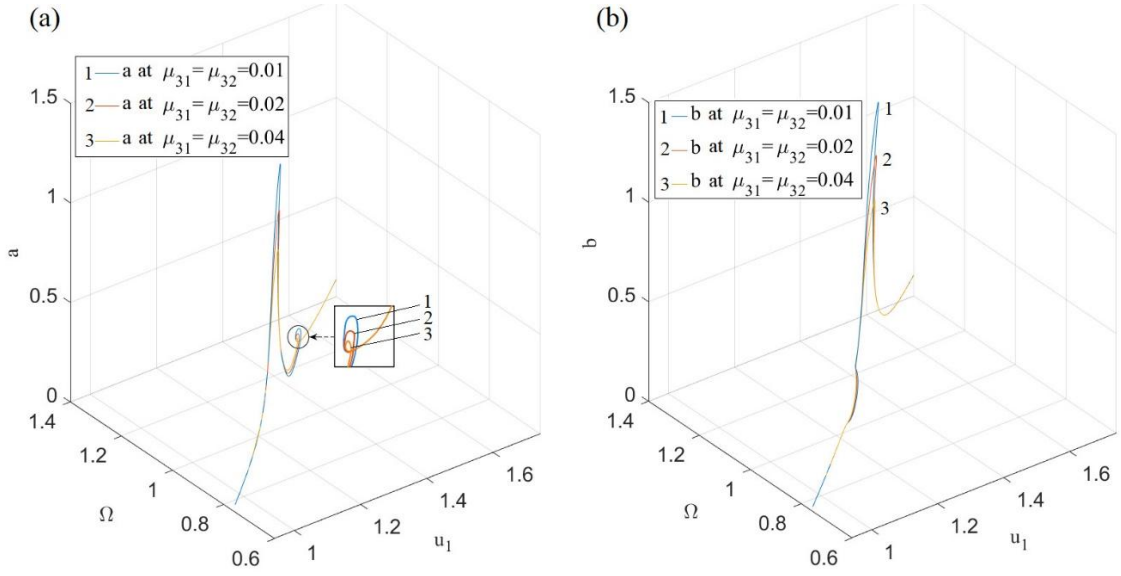

Figure 7. Stationary amplitudes a (a) and b (b) of oscillations at various values of the coefficient of cubic nonlinearity of damping.

On Figure 7b, the amplitude elevation of the first resonant region under the influence of nonlinearity of damping is so suppressed that it hardly differs from the main resonant curve. So, the graphs in Figures 6 and 7 show the overall picture of the non-ideal dynamics and the effect of linear damping and cubic nonlinearity of damping on them in the stationary mode.

Let's consider a special case when the rotor consistently gets stuck at both critical speeds. At values $K_3 = 0$ and $\mu_1 = 0.004,\ 0.006$ in velocity characteristics, a sequential double resonant capture

 doi:10.20944/preprints202605.1561.v1

with jumps is well noticed, and at $\mu_3 = 0.002$, $\mu_1 = 0.004$, effects at the boundary of the zones of two resonant captures are well noticed, at $\mu_1 = 0.004$ and $\mu_3 = 0.004,\ 0.006$, the Sommerfeld effect in the region of the first critical velocity will be eliminated.

The calculation results according to formulas (25) and (26) in the form of diagrams of the rotor vortex velocity Ω depending on the dimensionless voltage of the engine u_1 at various damping are shown in Figures 8. According to Figure 8a, two distinct jumps are observed (one for one direction at $\omega_{n1} = 1$, and the other for another direction perpendicular to the first one at $\omega_{n1} = 1.02$.

These two jumps are quite close to each other, which leads to resonance capture. The dotted lines in Figure 8a show the state of "no imbalance". In the mode of increasing the engine voltage, the 1st jump occurs at point "b" (i.e. u_1=1.280). This jump corresponds to the passage through the 1st resonance and should ideally position the rotational velocity at point "g*" lying on the dotted line. However, the velocity actually jumps from "b" and subsequently stops at point "g", since the system encounters the 2nd resonance zone much earlier, which prevents the transition to point "g". As soon as this happens, the rotor rotational velocity stops at the 2nd critical velocity prior to point "d" [6] corresponding to u_1=1.550 (i.e. the position in which the second jump occurs). After the second jump from "d" to "e", the dependence of velocity on voltage almost follows the linear trend indicated in equation $M = u_1 - u_2\varphi'$. If the resonant zones were not located one after the other, then the 1st jump would be quite simple (i.e. from "b" directly to "g*"). Instead, because of the back-to-back jump segments, the velocity trajectory traces from "b" to "g", then from "d" to "e" and finally from "e" onwards.

When the linear damping value increases from 0.004 to 0.006 (see Figure 8b), the size of the jumps along the Ω significantly decreased (from 1÷1.014 to 1÷1.011 in the first resonant region and from 1.020÷1.245 to 1.020÷1.174 in the second resonant region), but the phenomenon of sequential double resonant capture remained.

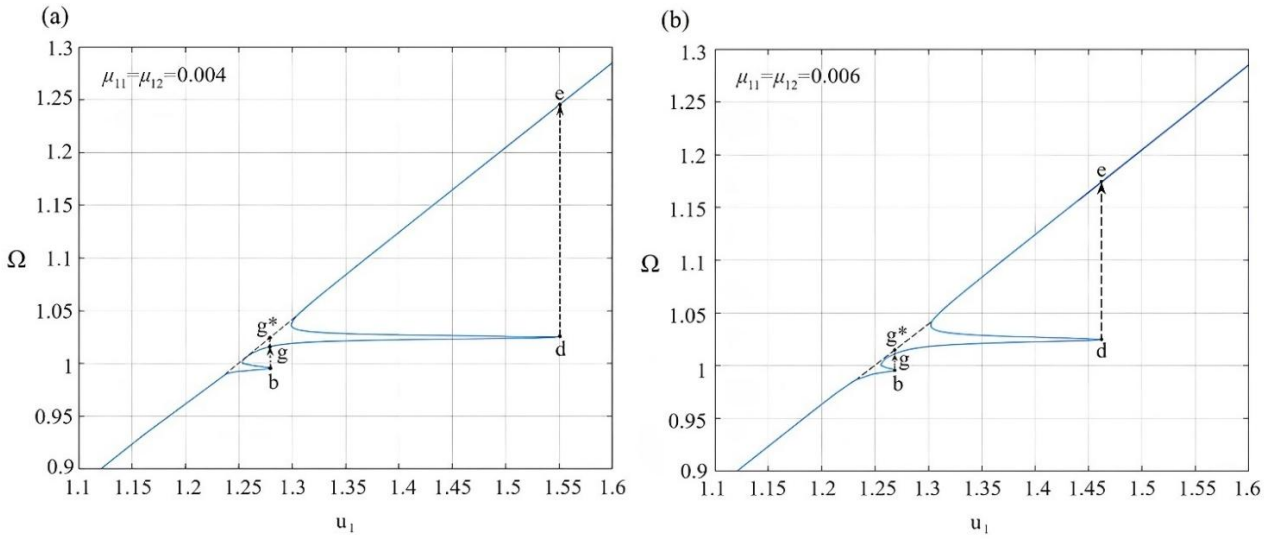

Figure 8. The speed characteristic of the rotor at different values of the linear damping coefficient.

Linear damping of 0.004 value enhanced with cubic nonlinearity of damping of 0.002 value (see Figure 9a) leads to displacement of the intersection point of the nonlinear jump line with the line of dependence of shaft rotation speed on motor voltage to the boundary of regions of two resonant captures, reduction of the sizes of unstable branches in resonant curves, significant reduction of the jump size in Ω from 1–1.014 to 1–1.010 in the first resonant region, from 1.020–1.245 to 1.020–1.086 in the second resonant region.

A comparison with the case of linear damping with a value of 0.006 also proves the predominant effect of nonlinearity of damping on reducing the values of unstable branches and, accordingly,

 doi:10.20944/preprints202605.1561.v1

reducing jump intervals. A further increase in the magnitude of the cubic nonlinearity of damping can eliminate the Sommerfeld effect with a jump, starting from the first resonant zone (Figure 9b).

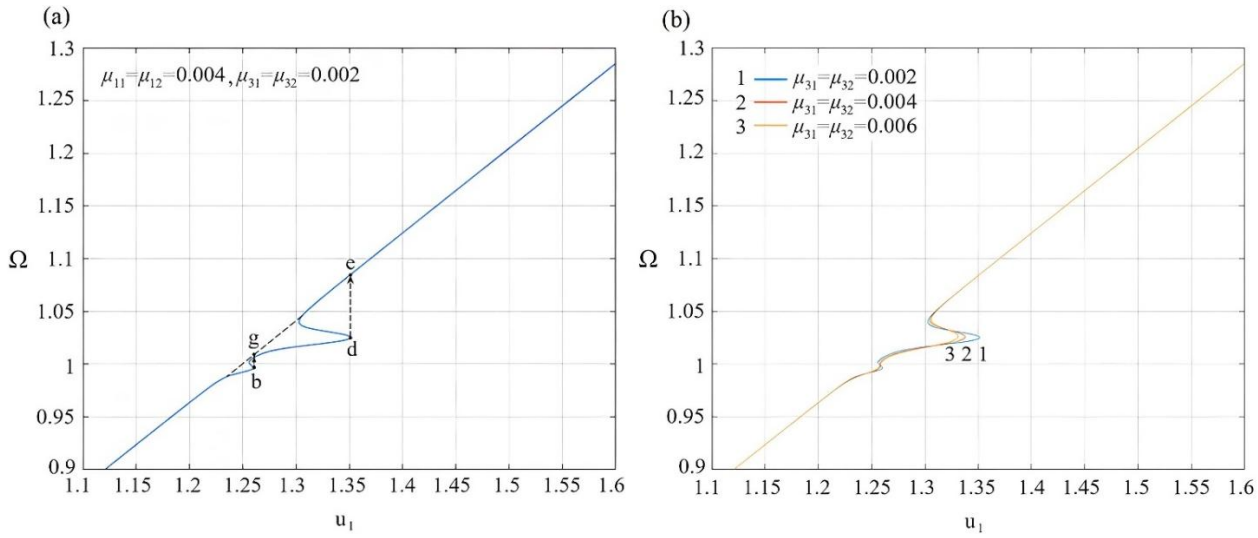

Figure 9. The speed characteristic of the rotor at different values of the coefficient of cubic nonlinearity of damping.

As a result of the strong interaction of the rotor system with a non-ideal energy source, loops appear in the resonant curves (Figure 10a) in areas bounded by jump lines, i.e. in bistability zones that do not exist in the ideal system (instead, there are elevations in the resonant curves). In the case of linear damping of values 0.004 and 0.006, the vertical size of the loop for the amplitude resonance curve $a=a(u_1)$ is significantly larger than the value of the maximum resonant amplitude. The second loop is located on the back of the amplitude resonance curve. Under the influence of cubic nonlinearity of damping of magnitude 0.002 with constant linear damping of magnitude 0.004, the dimensions of the loops in all directions have significantly decreased compared with the change in the magnitude of the maximum resonant amplitude (Figure 10b). The strong interaction of the system with the energy source affects the amplitude characteristics like a positive non-linear cubic stiffness of the elastic support, although it does not exist, bending the resonant curve and its loop to the right side. Under the influence of damping, the effect of the interaction of the excitation source with the rotor system is suppressed, the amplitude characteristic is straightened, decreasing in maximum dimensions.

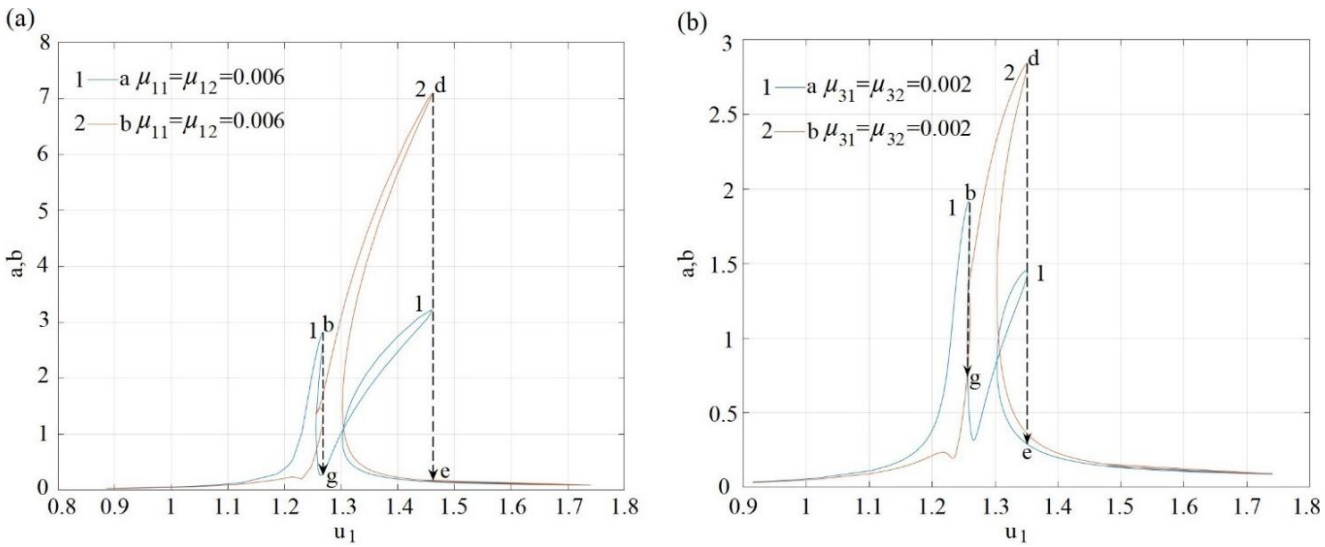

 doi:10.20944/preprints202605.1561.v1

Figure 10. The amplitude characteristic of the rotor at different damping values.

Now let's consider the case of the presence of a nonlinear cubic component of the stiffness of an elastic support. It is known that the nonlinear stiffness of the support not only preserves vibration isolation in the resonant region, but also transfers it to an area beyond the critical velocity [24]. As a result, the shaft rotation speed will not get stuck near the critical speed, but will increase with increasing voltage, the steeper the greater the value of nonlinear stiffness [30], thereby reducing the likelihood of the Sommerfeld effect. The angular velocity of the shaft reaching point b or d (Figure 2) jumps to a higher value. The curves of the amplitude characteristic stretch from the end and the greater the slope to the stress axis, the greater the nonlinear stiffness. With an increase in the damping value, the sizes of jumps and unstable branches are reduced [30], in the case of cubic nonlinearity of damping this is more significant.

3.2. Energy Resonant Passage and Damping Effects

In the dynamics of a non-ideal anisotropic gyroscopic rigid rotor, it is aimed to determine the control conditions for smooth and fast resonance escape using energies, linear damping and cubic nonlinearity of damping. To this end, following the methodology of works [1,14,46], the graphs of dissipated energy E_d as a function of shaft speed Ω are first plotted according to formula (33) at different values of linear damping μ_{11} and μ_{12} (Figure 11a) and cubic nonlinearity of damping μ_{31} and μ_{32} at constant linear damping $\mu_{11} = \mu_{12} = 0.01$ (Figure 11b). Near them, plots of motor energy E_m as a function of shaft angular speed Ω at different values of driven voltage u_1 are plotted using formula (32). The straight lines $E_m = E_m(u_1, \Omega)$ pass through the critical speed $\Omega = \omega_{n1} = 1$ and $\Omega = \omega_{n2} = 1.1$, through the peaks of the energy resonance curves $E_d = E_d(\Omega)$, that correspond to the values of the driven voltage u_{1b} and u_{1d} (Figure 2a and Figure 3a) at different values of linear damping and cubic nonlinearity of damping (Figure 2b and Figure 3b) and through points above the maxima of curves $E_d = E_d(\Omega)$. It should be mentioned that in [46] the approach was carried out using the total power and the power dissipated in the damping.

 doi:10.20944/preprints202605.1561.v1

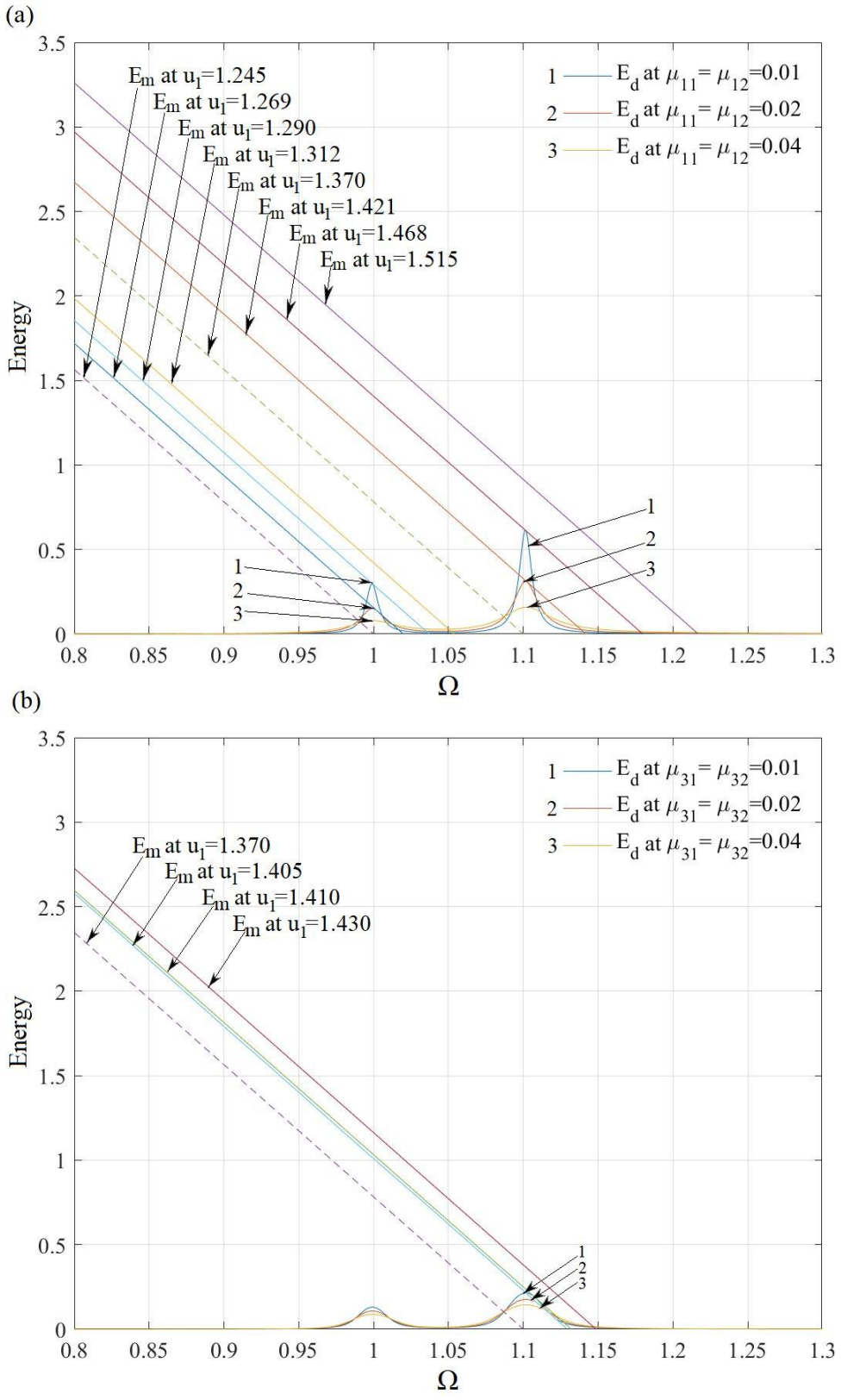

Figure 11. Energy depending on the speed of rotation of the shaft at different damping values.

In Figure 11a, in the first critical speed region, the source energy lines E_m for u_1=1.245 and E_m for u_1=1.269 intersect the dissipation energy line $E_d = E_d(\Omega)$ with $\mu_{11} = \mu_{12} = 0.01$ and these values of motor energy E_m are insufficient to overcome the first resonance region, therefore, rotor speed capture occurs, i.e., it is trapped in resonance for an indefinite time in both conditions, but straight

 doi:10.20944/preprints202605.1561.v1

line E_m at u_1 =1.269 for the case of $\mu_{11} = \mu_{12} = 0.02$ is a boundary line. Energy E_m at u_1 =1.290 for line $E_d = E_d(\Omega)$ with $\mu_{11} = \mu_{12} = 0.01$ is limiting, but for $\mu_{11} = \mu_{12} = 0.02$ it becomes sufficient for a smooth transition to the resonance region. The source energy E_m for u_1 =1.312 sufficiently provides smooth crossing of the first resonance region in the case of $\mu_{11} = \mu_{12} = 0.01$, and is quite a decent margin for passing the resonance region in other cases of $\mu_{11} = \mu_{12} = 0.02, 0.04.$ Equivalently, in the case of $\mu_{11} = \mu_{12} = 0.01$, the energy E_m with u_1 =1.515 is sufficient for smooth passage through the region of the second resonance, while in the case of $\mu_{11} = \mu_{12} = 0.02$ the energy E_m with u_1 =1.468 is even less.

Hence, the larger the damping value, the smaller the energy requirements of the force to smoothly pass the resonance curve region. In the case of $\mu_{11} = \mu_{12} = 0.04$ there is no Sommerfeld effect with nonlinear hops in the response of the dynamics (Figure 3). This supports the claim [2] that high damping often suppresses the Sommerfeld effect.

With a linear damping value of 0.01 supplemented with a cubic damping nonlinearity of 0.01, the Sommerfeld effect will only occur in the region of the second resonance, while it will be absent in the region of the first resonance (Figure 11b). Energy E_m at u_1 =1.370 and energy E_m at u_1 = 1.405 will not be sufficient to pass the second resonance region. Energy E_m at u_1 =1.410 is the limiting energy beyond which a smooth resonance passage can be achieved, for example, at E_m for u_1 =1.430.

Comparing the boundary energy of the smooth second resonance passage of the cubic nonlinearity of damping case of $\mu_{31} = \mu_{32} = 0.01$ at $\mu_{11} = \mu_{12} = 0.01$ (Figure 11b) with the same energy of the linear damping case at $\mu_{11} = \mu_{12} = 0.02$ (Figure 11a), we can see that the first case E_m at u_1 =1.410 is less than the second case E_m at u_1 =1.421, even without mentioning the unobstructed energy passage through the first resonance region in the nonlinearity of damping case.

Similar to the linear damping case (Figure 11a) the energy E_m at u_1 =1.405 for curve $E_d = E_d(\Omega)$ with $\mu_{31} = \mu_{32} = 0.04, \mu_{11} = \mu_{12} = 0.01$ is threshold, the energy E_m at u_1 =1.410 for curve $E_d = E_d(\Omega)$ with $\mu_{31} = \mu_{32} = 0.02, \mu_{11} = \mu_{12} = 0.01$ is threshold, but for the case of $\mu_{31} = \mu_{32} = 0.02, \mu_{11} = \mu_{12} = 0.01$ it is sufficient for free resonant passage.

It can therefore be argued that in the resonant regions, the larger the damping effect, the less energy of the resonant oscillations goes to dissipation. Therefore, amplifying the predominantly with cubic nonlinearity of damping is an effective model of optimal damping and one of the resonant amplitude control methods for smooth passages.

3.3. Transient Response and Damping Effects

The results of solving the system of equations (23) and direct modeling of the equations of motion of the rotor (14) are almost the same. The rate of change of the drive voltage over time was 0.00025. The transient response during acceleration at various values of linear damping and nonlinearity of damping is shown in Figures 12 and 13.

 doi:10.20944/preprints202605.1561.v1

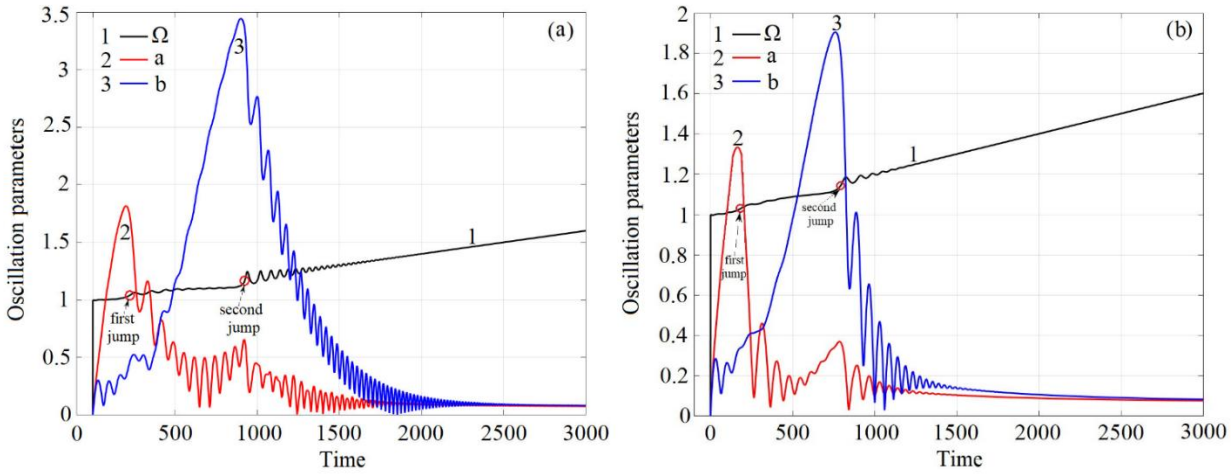

Figure 12. Transient response during acceleration at: (a) $\mu_{11}=\mu_{12}=0.01$, (b) $\mu_{11}=\mu_{12}=0.02$.

In the first resonant region, the angular shaft speed Ω, equal to 1, practically does not change (Figure 12a) or changes slightly (Figure 12b and Figure 13), while the oscillation amplitudes increase steeply, when the rotation speed jumps to a higher value of the oscillation amplitude, they fall sharply to rather low values (first jump). Further, the angular velocity of the shaft remains unchanged (Figure 12a) or slightly changed (Figure 12b and Figure 13) until the value Ω=1.1 is reached, and at the next jump of the shaft rotation speeds to a higher value, the oscillation amplitude fall to significant low values (second jump). With an increase in the linear damping value from 0.01 to 0.02, the maximum amplitudes of the resonant regions significantly decreased, the right boundary of the jump effect in Ω also decreased in time: 250 to 221 in the first resonant region, and 971 to 794 in the second resonant region. If we compare the results of damping the maximum resonant amplitudes at $\mu_{11}=\mu_{12}=0.02$ (Figure 12b) and $\mu_{31}=\mu_{32}=0.01$, $\mu_{11}=\mu_{12}=0.01$ (Figure 13), then the combined damping option is advantageous.

The maximum resonant amplitudes in magnitude in the combined version are less than in the case of linear damping. The right boundary of the jump effect in time in the first resonant region corresponds to 177 against 221. This means that when choosing operating speeds beyond critical speeds, the increase in linear damping with cubic non-linearity of damping significantly expands the range of operating speeds towards lower values.

It should be noted that when the rotor velocity is fixed at the stability threshold, the steady-state amplitude of the swirl is not constant due to the mixing of steady-state synchronous and asynchronous swirls occurring with two different frequencies [42].

The concepts of stability of stationary modes of motion, the dependency of steady states on the energy source properties, the concepts of hops in oscillations on the boundary of stability regions, identified through the analysis of equations (23), will be qualitatively suitable for characterizing stationary resonance processes. This makes it possible not to engage in a detailed analysis of stability criteria and only to consider the specifics of the rotor system [1]. Proceeding from this, in the stability criterion used in the article [42], the designations of the maximum power (30): $N_m(\Omega)$ and power for damping oscillations (31): $N_d(\Omega)$ multiplied by the time differential $d\bar{t}$ and by integrating the obtained expression in the time interval of period $2\pi/\Omega$, the following is obtained

$$\frac{d}{d\Omega}\left[E_m(\Omega)-E_d(\Omega)\right]\prec 0, \tag{32}$$

 doi:10.20944/preprints202605.1561.v1

where $E_{\mathrm{m}}(\Omega)$ and $E_{\mathrm{d}}(\Omega)$ are defined by formulas (32) and (33). The concept of the derivative sign (34) may be obtained by considering the mutual arrangement of the graphs $E_m(\Omega)$ and $E_d(\Omega)$ [1,24]. As shown in Figure 14, this derivative is negative at the points of sections ba•, gh, dc• and ef. Condition (32) is fulfilled at the points of sections bh and df, but the condition of relative stability with respect to the variable Ω [1] is not fulfilled and their product becomes positive. Therefore, the stability criterion (32) is realized at points of curves ba, gh, dc, and ef. The points b and h, d and f in Figure 14 may match the similar points in Figure 4a at μ_{11}=μ_{12}=0.01.

Increasing the linear damping value from $\mu_{11}=\mu_{12}=0.01$ to $\mu_{11}=\mu_{12}=0.02$ will reduce the size of the instable branch that corresponds to the instable mode of stationary oscillations by u_1 from 1.266÷1.290 to 1.267÷1.269 (by Ω from 1.017÷1.036 to 1.018÷1.019) in the first resonance zone, and by u_1 from 1.399÷1.468 to 1.407÷1.421 (by Ω from 1.124÷1.179 to 1.130÷1.141) in the second resonance zone. Combining linear damping $\mu_{11}=\mu_{12}=0.01$ with cubic non-linearity of damping $\mu_{31}=\mu_{32}=0.01$ reduces the size of the instable branch in the second resonance zone by u_1 to 1.406÷1.410 (by Ω to 1.129÷1.133), which is significantly less than in the case of the linear damping value with $\mu_{11}=\mu_{12}=0.02$.

With a small polar moment of inertia of the rotor, in order to reduce the acceleration of the transient process, it is proposed to slow down the variation in the angular velocity of rotation of the shaft by the damping method with a slow change in the driven angular velocity of the motor. From Figure 15, it can be seen that the angular velocity of the shaft fluctuates around its average value, equal to the value of the driven motor speed, with a fairly significant amplitude. By increasing the damping value from 0.01 to 0.02, one can significantly suppress the amplitude of shaft rotation speed oscillations. It is possible to enhance the effect of damping by complementing linear damping with cubic non-linearity of damping. From Figure 16, it can be seen that linear damping amplification with cubic non-linearity of damping is much more effective in suppressing the amplitude of shaft angular velocity oscillations than with increasing linear damping by an amount equal to the value of non-linearity of damping.

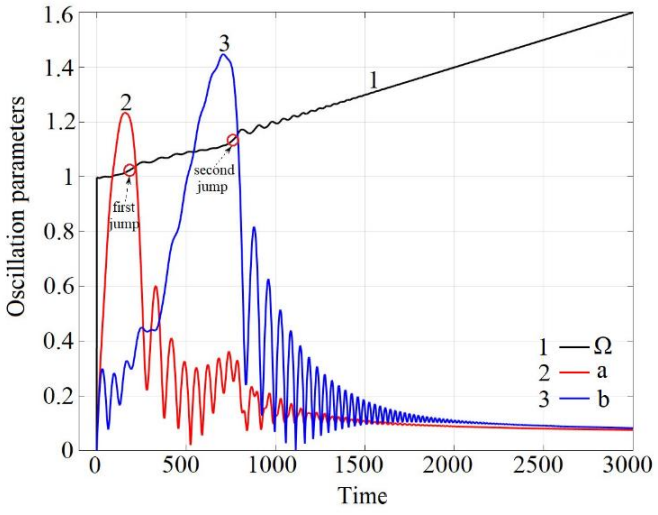

Figure 13. Transient response during run-out at $\mu_{31}=\mu_{32}=0.01$ and $\mu_{11}=\mu_{12}=0.01$.

 doi:10.20944/preprints202605.1561.v1

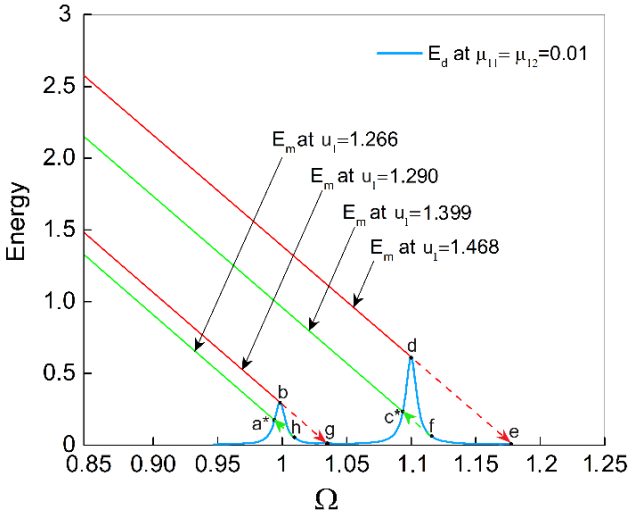

Figure 14. Dependence diagrams of $E_m(\Omega)$ and $E_d(\Omega)$ for rotor system.

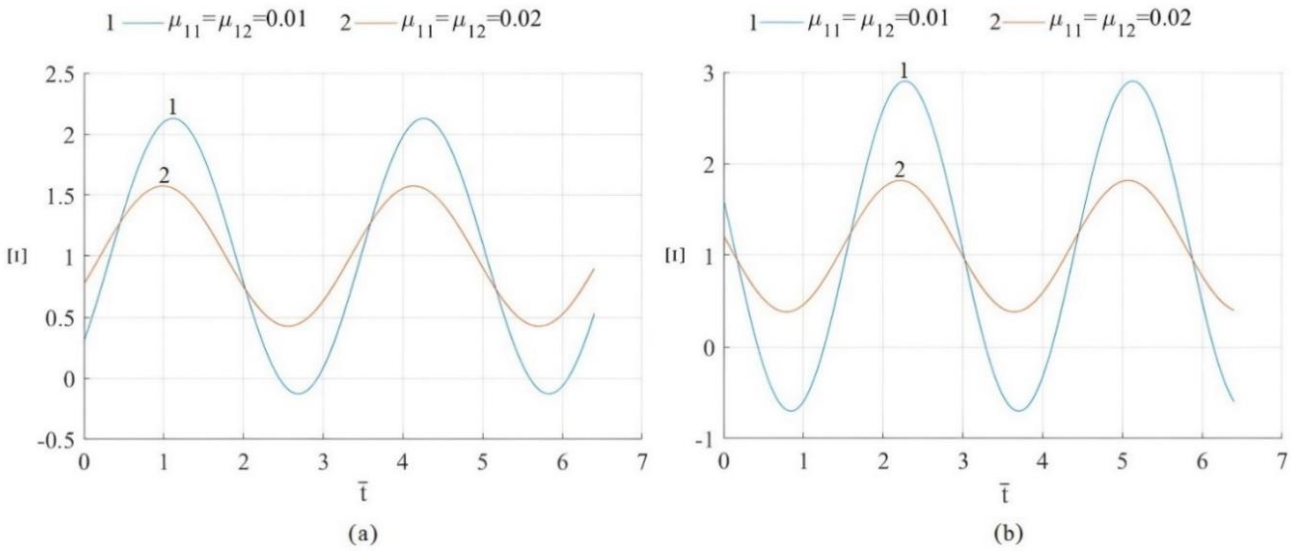

Figure 15. Angular speed of rotation of the shaft as a function of time at various values of linear damping for: (a) $\Omega = \omega_{n1} = 1$, (b) $\Omega = \omega_{n2} = 1.1$.

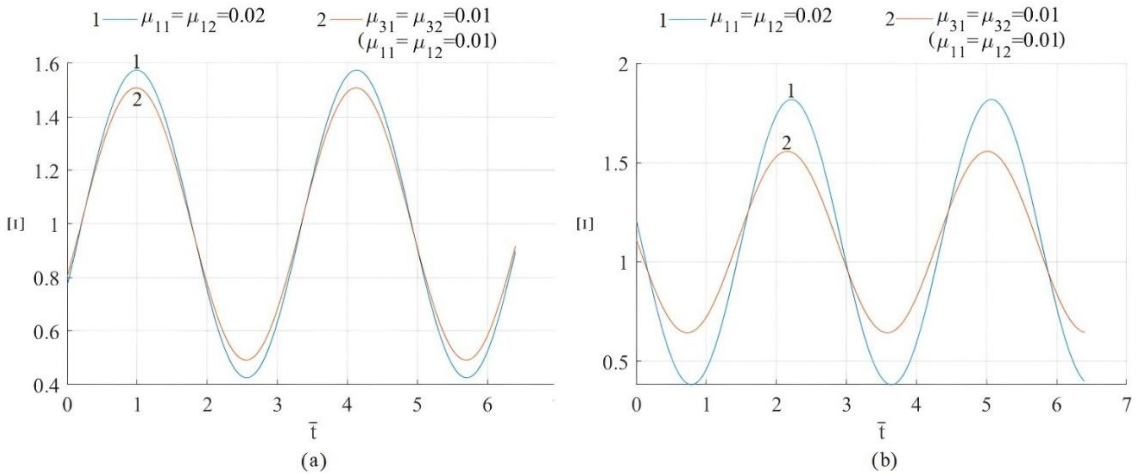

Figure 16. Angular speed of rotation of the shaft as a function of time at various values of damping for: (a) $\Omega = \omega_{n1} = 1$, (b) $\Omega = \omega_{n2} = 1.1$.

 doi:10.20944/preprints202605.1561.v1

4. Experimental Studies of the Dynamics of a Non-Ideal Anisotropic Gyroscopic Rotor of a Centrifuge

Experimental studies of the dynamics of a gyroscopic rotor system with a viscoelastic support with anisotropic restoring and damping characteristics were carried out on an experimental centrifuge setup, the general appearance of which is shown in Figure 17, and the layout of the elastic damping sheet inserts is shown in Figure 18.

The rotor is made in the form of a cylindrical cup in order to satisfy the condition that the moment of inertia about a diametral axis exceeds the moment of inertia about the polar axis. The cup is mounted at the upper end of a shaft connected to the motor rotor shaft through coupling with a bearing, supported by elastic damping inserts. The viscoelastic material sheets are tightly fitted in the grooves of the sides of a regular hexagon (Figure 18a), and provision is made for replacing them with other elastic-damping properties. Anisotropy of the elastic-damping properties of a support in orthogonal directions can be created by placing a viscoelastic material with some properties in the corner grooves of the diagonal of the supporting quadrilateral, and in the corner grooves of a perpendicular diagonal of a similar material with other properties (Figure 18b). The lower end of the motor rotor shaft, rigidly mounted inside the cylindrical casing, is supported by a cardan support. An encoder is attached to the lower part of the motor to provide feedback to the control stand. Overall, the installation housing is fastened to the lower platform.

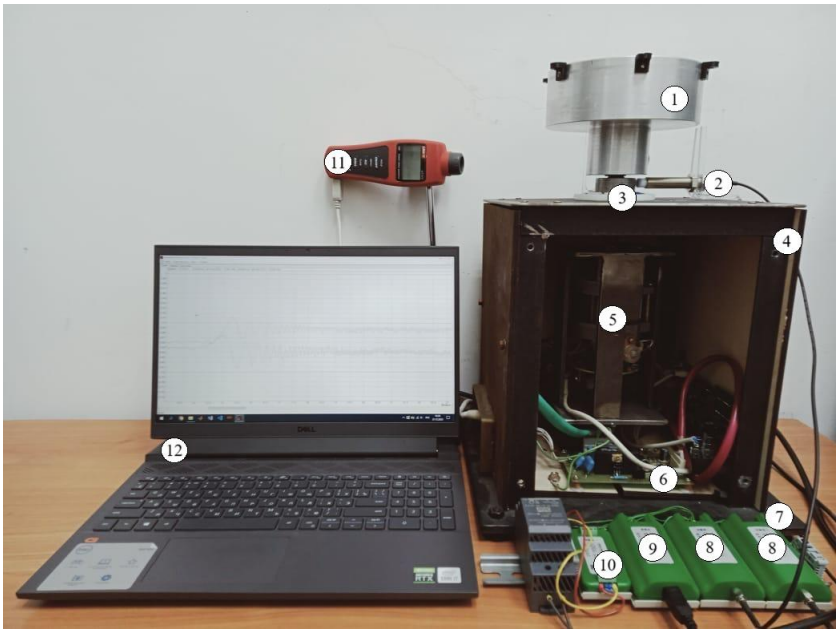

Figure 17. General view of the experimental centrifuge: 1 – rotor cup, 2 – ZET 701 probes, 3 – viscoelastic support, 4 – housing, 5 – electric motor with shroud, 6 – control stand, 7 – platform, 8 – ZET 7140-S eddy-current displacement sensor, 9 – ZET 7001-P measuring-line connector, 10 – ZET 7174 interface converter, 11 – UNI-T UT372 tachometer, 12 – laptop.

 doi:10.20944/preprints202605.1561.v1

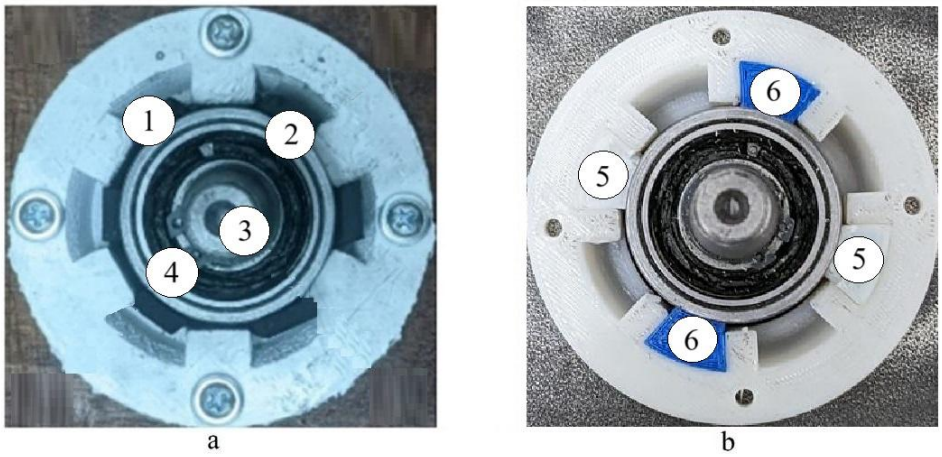

Figure 18. Design of the viscoelastic support a – based on a hexagon: 1 – rubber sheets (OaGRR or HTAAR brands), 2 - coupling, 3 - rotor shaft, 4 - bearing; b – based on a quadrilateral: 5 – viscoelastic sheet inserts, HIPS brand, 6 - viscoelastic sheet inserts, BFLEX brand.

The main elements of the setup have the following parameters. The rotor cup has mass m=1.053 kg, weight G=10.33 N, polar moment of inertia $J_P = 0.05\ kgm^2$, diametral moment of inertia $J_D = 0.08\ kgm^2$, and eccentricity e_r=1.1*10^{-3} m. The bearing span is l_2=0.260 m, and the distance from the lower support to the cup center is l_1= 0.360 m. Support stiffness coefficients are as follows: for OaGRR brand rubber (oil and gasoline resistant rubber) $k_1 = 25.760*10^3\ N*m^{-1}$ during rotor run-up and, $k_1 = 208.500*10^3\ N*m^{-1}$ during rotor run-down, for HTAARR brand rubber (heat-temperature-acid-alkali resistant rubber) $k_1 = 38.150{\cdot}10^3\ N{\cdot}m^{-1}$ during rotor run-up and, $k_1 = 189.400{\cdot}10^3\ N{\cdot}m^{-1}$ during rotor run-down; for viscoelastic material grade BFLEX $k_{11} = 3.295*10^3\ N*m^{-1}$, for viscoelastic material grade HIPS (high impact polystyrene) $k_{12} = 306.809*10^3\ N*m^{-1}$. The motor constant is $c_M\Phi_M$=0.4 NmA^{-1}, and the electrical resistance of the motor rotor is R=4 Om.

To measure the transverse displacement of the shaft, a ZET 701 probe is installed at the top of the housing; it is connected to the ZET 7140-s eddy-current displacement sensor, which in turn is connected to the ZET 7001-R measuring-line connector and then to the ZET 7174 interface converter. The interface converter is connected to a computer. A UNI-T UT372 tachometer is used to measure the rotational speed. The amplitude-time (and amplitude-frequency) characteristic is determined by the envelope of the oscillogram of the transverse movement of the shaft, recorded and displayed on the computer display [47]. In the video material [47] demonstrates the corresponding oscillogram of the transverse movement of the shaft, obtained during the acceleration of the rotor in the case of using a support material made of OaGRR rubber

During the measurement procedures, the ZETLAB [48 eddy-current sensor software and the UT372 tachometer software will be used. The results of the experimental work are recorded in the ZETLAB [48] program. The measured data are processed in MatLab. The experimental setup during operation is shown in Figure 19 and video [47].

 doi:10.20944/preprints202605.1561.v1

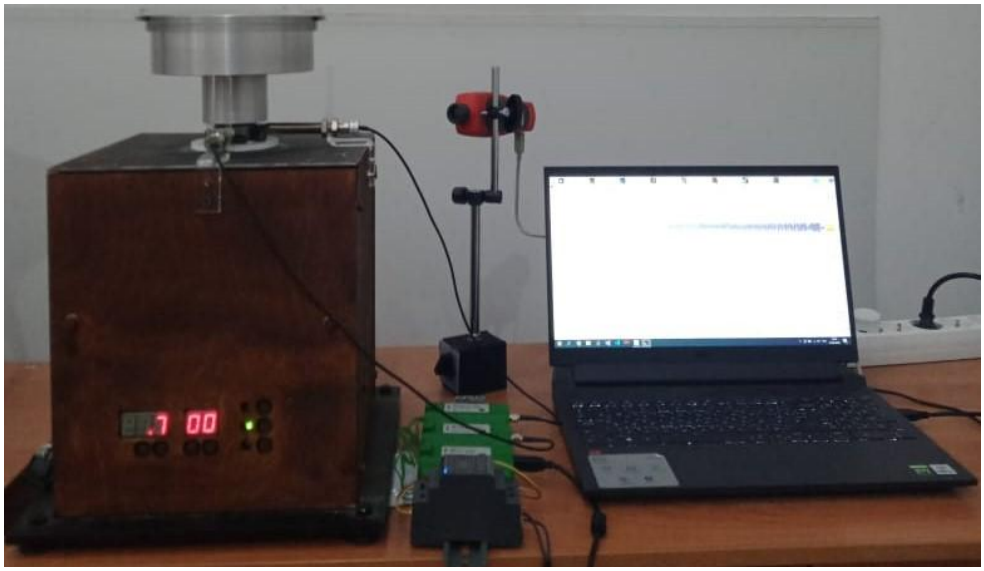

Figure 19. Test stand during operation.

The experimental nonstationary amplitude characteristics of a gyroscopic rotor with an elastic hexagonal support, obtained with a limited-excitation motor and shown in Figures 20 and 21, are very similar to the corresponding characteristics reported in [49,50] for an ideal-excitation motor. The results presented in [30] indicate that, for the stiff support-stiffness characteristic typical of many systems, the resonant vibration amplitudes at different damping values and with a non-ideal energy source slightly exceed the corresponding values obtained for a system with an ideal energy source. In the case of an ideal energy source, the amplitude-time-frequency characteristic of the rotor run-up with a support made using HTAARR rubber has a zigzag change in amplitude after resonance [49], [Figure 12, curve X2]. This effect is due to the superposition of the natural and forced oscillations of the rotor [42,44,49]. Under non-ideal excitation conditions, the experimental amplitude-time-frequency characteristic of the rotor acquired a form corresponding to a stationary oscillatory mode (Figure 20, curve X2). This indicates that with a slow increase in the excitation frequency, the system exhibits behavior that is increasingly close to a stationary amplitude-frequency characteristic.

In the hexagonal supports, the insert plates were cut from rubber brands OaGRR and HTAARR. The critical speed of accelerated rotor whirl is 102.2 s-1 for OaGRR brand rubber and 124.4 s-1 for HTAARR brand rubber (Figure 20), while the critical speed of decelerated rotor whirl is 290.9 s-1 for OaGRR brand rubber and 277.3 s-1 for HTAARR brand rubber (Figure 21). These experimental critical-speed values practically coincide with the analytically determined values obtained from formula (33) [20,44]:

$$\omega_0 = \sqrt{\frac{k_1 l_2^2 - mgl_1}{ml_1^2 - (J_P - J_D)}} \tag{33}$$

The difference in the rotor critical-speed values during run-up and run-down is explained, as in Bharti et al. [14], by asymmetry in the support stiffness and shaft flexibility.

When the grade of the viscoelastic support plate is changed, the stronger damping effect of HTAARR brand compared with that of OaGRR brand is readily observed. The maximum amplitude corresponding to the critical run-up speed decreases from 1.249 mm to 1.169 mm. During run-down, the resonant amplitude decreases from 1.233 mm to 1.146 mm, and in the inter-resonance zone the vibration amplitude decreases from 1.140 mm to 1.090 mm. The vibration amplitudes at the critical speeds during run-down are lower than during run-up [14]. In the resonance zone during run-down, jump phenomena are observed, indicating the existence of a nonlinear hardening stiffness characteristic of the support. Comparison of the resonance curves in Figures 20 and 21 confirms stiffness asymmetry in opposite directions.

 doi:10.20944/preprints202605.1561.v1

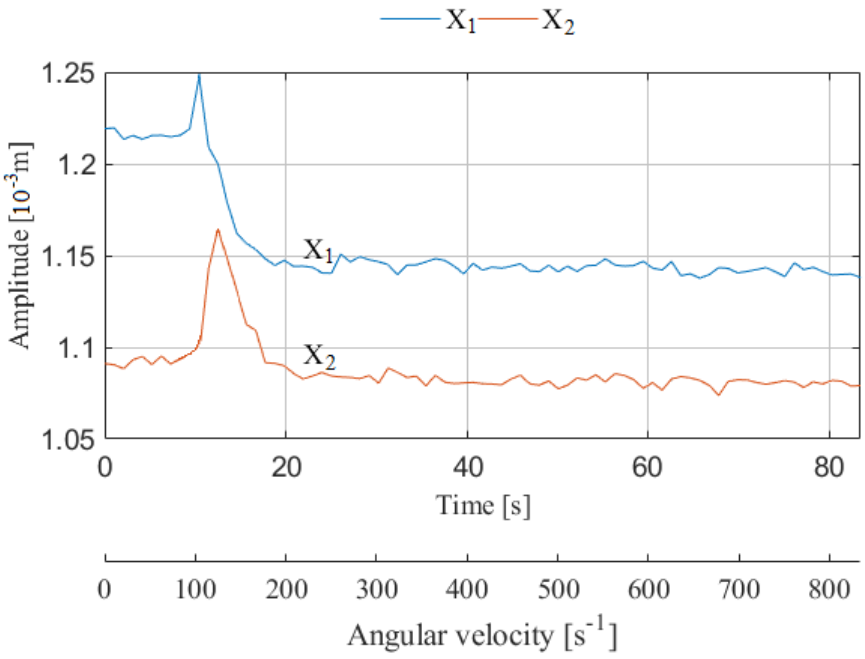

Figure 20. Experimental amplitude-time-frequency curves of gyroscopic rotor run-up for different support materials: X_1 – for OaGRR brand rubber, X_2 – for HTAARR brand rubber.

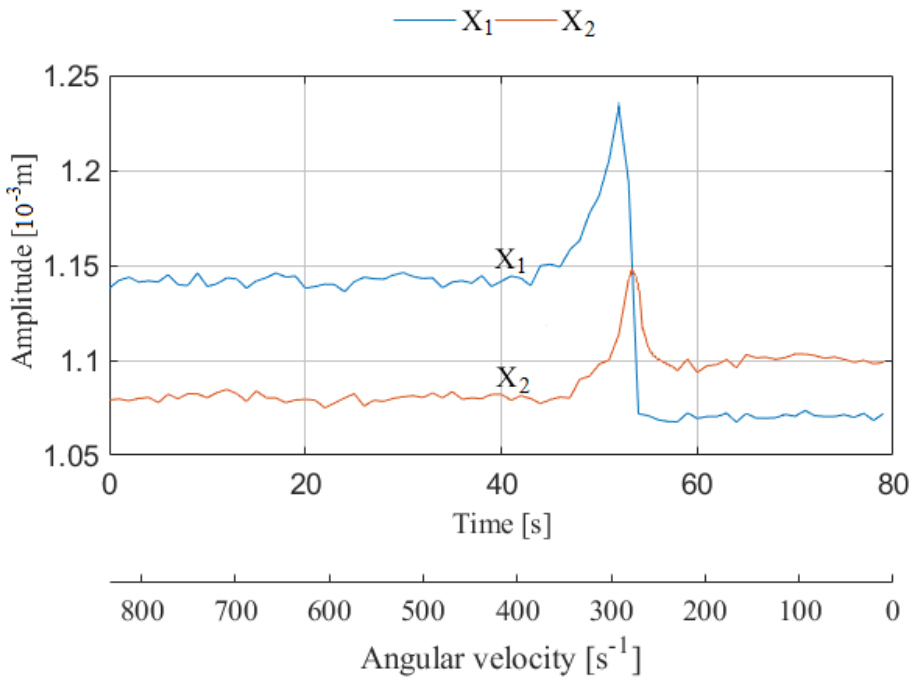

Figure 21. Experimental amplitude-time-frequency curves of gyroscopic rotor run-down for different support materials: X_1 – for O&GLR brand rubber, X_2 – for HTAAR brand rubber.

To numerically describe the damping effect of the material, the values of the linear damping coefficient and the cubic damping nonlinearity were approximately determined from the intersection points of the experimentally and analytically obtained run-up amplitude characteristics of the rotor. In the resonance regions, the values of the linear damping coefficient and the cubic damping nonlinearity are approximately: μ_{d1}=9.03 *Nms*, μ_{d3}=36.71 Nms^3 for OaGRR brand rubber, and μ_{d1}=9.75 *Nms*, μ_{d3}=48.83 Nms^3 for HTAARR brand rubber. A comparison of the damping coefficients for the two rubber grades shows that suppression of vibration amplitude in the resonance regions occurs

 doi:10.20944/preprints202605.1561.v1

mainly under the influence of the cubic damping nonlinearity. The same effect is observed in the post-resonance shaft-speed range.

Thus, taking into account the results reported in [20,32,41,46], it can be concluded that if, in the pre-resonance region, amplitude suppression is a consequence of linear damping, and in the resonance region it results from the combined effect of linear damping and cubic damping nonlinearity, then in the post-resonance regions it is due solely to the effect of the cubic damping nonlinearity.

Under support-material stiffness asymmetry, the rotor's nonstationary speed characteristics were constructed from the solutions of the differential equations describing nonstationary transient processes:

$$\begin{aligned}
\frac{d\omega}{dt} &= \frac{1}{J_P}\left[\frac{c_M\Phi_m}{R}U-\left(\frac{c_Mc_E\Phi_m^2}{R}+q_{rm}\right)\omega+me_r\omega\omega_0 l_1\sin\chi\right],\\
\frac{da}{dt} &= -\frac{me_r l_1\omega^2}{2\left(ml_1^2+J_D\right)\omega_0}\sin\chi-\frac{\mu_{dp1}a}{2\left(ml_1^2+J_D\right)}-\frac{3\mu_{dp3}\omega_0^2a^3}{8\left(ml_1^2+J_D\right)},\\
\frac{d\chi}{dt} &= \omega_0-\omega-\frac{me_r l_1\omega^2}{2\left(ml_1^2+J_D\right)\omega_0 a}\cos\chi+\frac{3k_3l_2^4a^2}{8\left(ml_1^2+J_D\right)\omega_0}.
\end{aligned} \tag{34}$$

To solve system (34), the initial conditions must be known: the shaft angular velocity ω, the amplitude a, the initial phase χ, and the motor voltage U. These are determined from the steady-state oscillation equations, i.e., from the steady-state amplitude-frequency and phase-frequency characteristics and the control equation:

$$\begin{aligned}
&\left\{\left[2\left(ml_1^2+J_D\right)\left(\omega_0-\omega\right)+\frac{3}{4\omega_0}k_3l_2^4a^2\right]^2+\left(\mu_{dp1}+\frac{3}{4}\mu_{dp3}\omega_0^2a^2\right)^2\right\}\omega_0^2a^2=\left(me_rl_1\omega^2\right)^2,\\
&tg\chi=-\frac{\mu_{dp1}+\frac{3}{4}\mu_{dp3}\omega_0^2a^2}{2\left(ml_1^2+J_D\right)\left(\omega_0-\omega\right)+\frac{3}{4\omega_0}k_3l_2^4a^2},\\
&\frac{c_M\Phi_m}{R}U-\left(\frac{c_Mc_E\Phi_m^2}{R}+q_{rm}\right)\omega+\frac{a^2\omega_0^2}{\omega}\left(\mu_{dp1}+\frac{3}{4}\mu_{dp3}\omega_0^2a^2\right)=0.
\end{aligned} \tag{35}$$

and were matched to the experimental data in Figure 20. For O&GLR brand at t=0: $\omega=\omega_0$=102.2 s^{-1}, a=1.249*10^{-3} m, χ= -π/2, U=40.97 V; for HTAARR brand at t=0: $\omega=\omega_0$=124.4 s^{-1}, a=1.169*10^{-3} m, χ= -π/2, U=49.87 V.

Figure 22 shows the speed characteristics for accelerated rotor whirl with supports made of O&GLR brand rubber (1) and HTAAR brand rubber (2)

 doi:10.20944/preprints202605.1561.v1

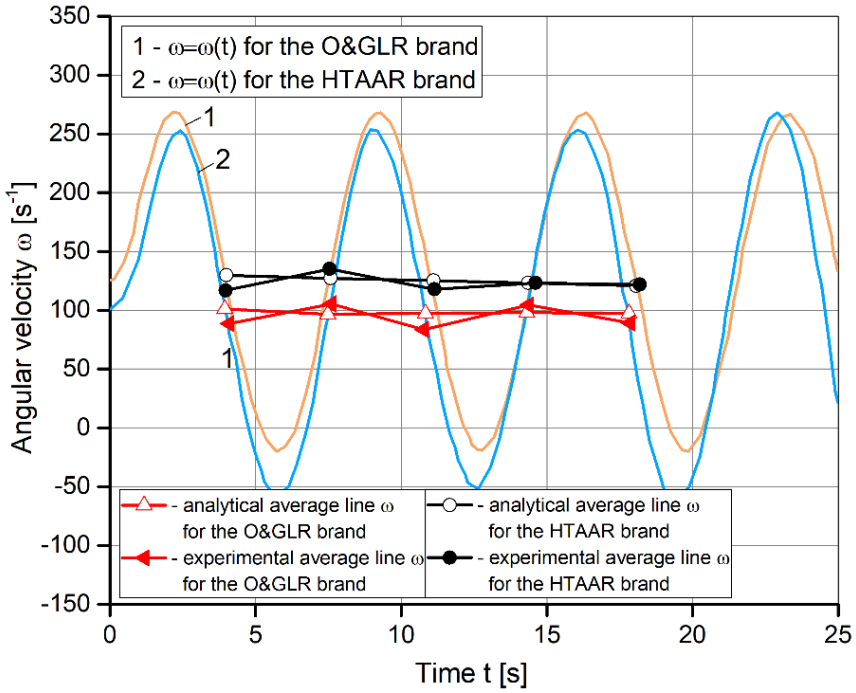

Figure 22. Capture of the shaft angular velocity during rotor run-up with supports: 1 - BMS rubber brand, 2 - HTAAR rubber brand.

At the critical values, the rotor-shaft angular velocity exhibits an oscillatory process over time about these nearly constant values. The rotor system remains in this state until the supplied power becomes sufficient to pass through it (the Sommerfeld effect). The magnitude of the variation in rotor whirl speed depends on the motor voltage U. When the motor voltage varies slowly according to $U=U_0+\nu t$, where $\nu<<1$, at the initial time the voltage U and the variation of the angular velocity ω remain unchanged (Figure 22). At a constant motor voltage $U=U_0$ the theoretical and experimental average values of the rotor swirl velocity variation lie near the lines determined by the critical values. The oscillation amplitudes of the angular velocity ω at the critical speeds are fairly large, comparable to the mean critical-speed values, which confirms that the oscillogram - i.e., measurement of ω variation - was taken precisely at the critical speed values. Satisfactory agreement between the analytical and experimental results can be observed (Figure 22).

Stiffness and damping anisotropy in mutually perpendicular directions was created by placing high-impact polystyrene (HIPS) in the corner cells along one diagonal of the quadrilateral (octagonal) support, and flexible soft material BFLEX in the corner cells along the other diagonal. The experimental amplitude-time-frequency characteristics of the rotor for the vibration directions $x(\alpha)$ and $y(\beta)$ are shown in Figure 23. The first critical speed is ~31.8 s^{-1} for one direction, and the second critical speed is ~318.2 s^{-1} for the other direction perpendicular to the first. These experimental critical-speed values coincide with the values found analytically in accordance with expression (11) using the following formula:

$$\omega_{1,2}=\left\{\frac{\left(J_D+ml_1^2\right)\left[\left(k_{11}l_2^2-mgl_1\right)+\left(k_{12}l_2^2-mgl_1\right)\right]}{2\left[\left(J_D+ml_1^2\right)^2-J_P^2\right]}\mp\left\{\frac{\left(J_D+ml_1^2\right)^2\left[\left(k_{11}l_2^2-mgl_1\right)+\left(k_{12}l_2^2-mgl_1\right)\right]^2}{4\left[\left(J_D+ml_1^2\right)^2-J_P^2\right]^2}-\frac{\left(k_{11}l_2^2-mgl_1\right)\left(k_{12}l_2^2-mgl_1\right)}{\left(J_D+ml_1^2\right)^2-J_P^2}\right\}^{\frac{1}{2}}\right\}^{\frac{1}{2}} \quad (38)$$

Direction $x(\alpha)$ is the principal direction for the lower critical speed, whereas direction $y(\beta)$ is the principal direction for the higher critical speed. Consequently, the vibration amplitude in direction

 doi:10.20944/preprints202605.1561.v1

$x(\alpha)$ at the lower critical speed is greater than the corresponding amplitude at the higher critical speed, while the vibration amplitude in direction $y(\beta)$ at the lower critical speed is smaller than the corresponding value at the higher critical speed. The difference between the resonant vibration amplitudes for a given direction is explained by the influence of the projections of the passive gyroscopic moment and by the difference in support stiffness in orthogonal directions. Instead of the slopes of the main resonance curves and the loops or humps of the secondary vibration amplitudes present in the analytically constructed amplitude-time characteristics for these directions, the presence of experimental jump lines proves the nonlinearity inherent in the complex nature of the support's orthogonal stiffness anisotropy. In experiments, jump transitions are usually observed instead of bistable segments of resonance curves [19]. In the first resonance region, jumps occur from a large amplitude and lower rotational speed to a smaller amplitude and higher rotational speed, whereas in the second resonance region the jump transitions proceed from a smaller amplitude and rotational speed to a larger amplitude and higher shaft speed. This confirms anisotropy of the nonlinear stiffness of the elastic support material: if, in direction $x(\alpha)$, the support's nonlinear elasticity exhibits a hardening characteristic, then in direction $y(\beta)$ it exhibits a softening characteristic. The manifestation of damping anisotropy, including geometrically nonlinear damping, in the region beyond the critical rotational speeds is somewhat more pronounced than in the region between the critical shaft speeds.

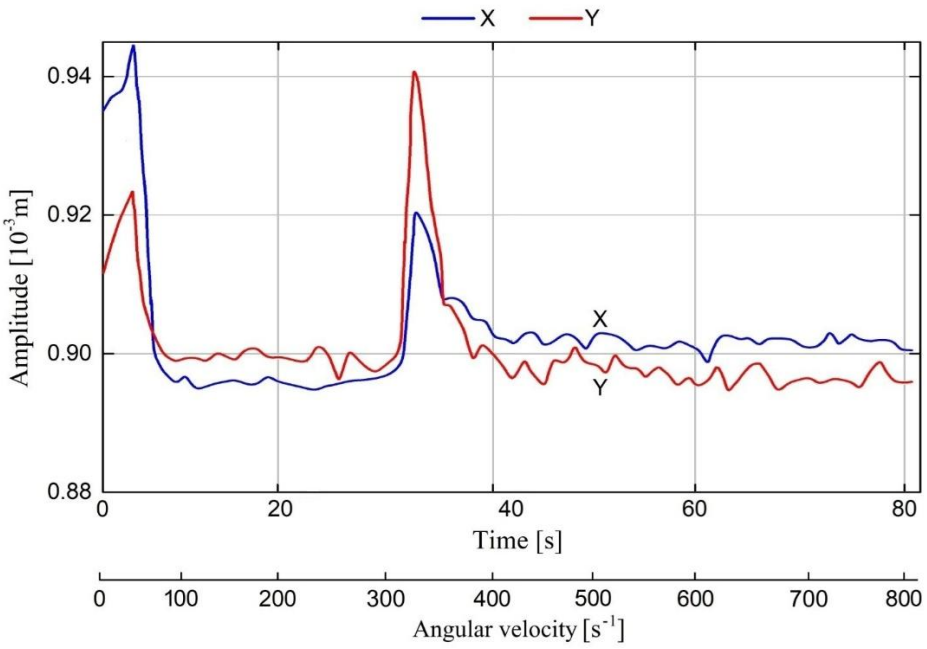

Figure 23. Resonance amplitude-time characteristics during gyroscopic rotor run-up under anisotropy of the support material's elastic-damping properties in mutually perpendicular directions: X(α) and Y(β).

5. Conclusions

Nonlinear dynamics responses of an anisotropic gyroscopic rotor with linear damping and cubic nonlinearity of damping, driven by a non-ideal motor with dynamic torque proportional to the shaft speed, are studied.

As solutions to the differential equations of rotor motion, the equations of non-stationary transitions are obtained, from there the control equation with the reduced voltage in connection with the stationary frequency transient characteristics, from the control equation the ratio of moments, the ratio of powers and energies. This is certainly a significant advantage of the method of small disturbance theory in covering solutions to a wide range of problems.

 doi:10.20944/preprints202605.1561.v1

It is established that combining linear damping with amplification of the nonlinear cubic component can cause the disappearance of the unstable branch in the first reso-nance region and a significant reduction in the size of the jump in the shaft rotation speed in the second resonant region. Further increase of this damping component may virtually destroy the Sommerfeld effect.

The results of the intense interaction between the system and the motor were reflected in the slope of the resonance curves in the absence of a nonlinear component of the support rigidity and the manifestation of loops in the critical speed regions. As a result of the effect of cubic nonlinearity of damping, the maximum resonant amplitudes are suppressed more strongly, and the loops decrease in size and turn into amplitude elevations of the resonant curves than as a result of linear damping.

It is proven that the greater the effect of damping, the less energy (power) will be required for the drive to move smoothly through the critical speed regions and the wider the operating speed range is. Linear damping combined with cubic nonlinearity of damping is an effective model of optimal damping and one of the resonant amplitude control methods for smooth passages.

6. Patents

Based on the theoretical studies presented in [29,43,45] and in the present research, a three-dimensional model [51] was developed in the SolidWorks environment, and a laboratory centrifuge setup (Figures 17 and 19, [47]) based on a vertical gyroscopic rotor was built. This setup was patented as an invention [52] at the Eurasian Patent Office and introduced into research practice. Experimental studies were performed on the dynamics of a rigid gyroscopic rotor with anisotropic stiffness of the elastic support, characterized by viscous linear damping and cubic nonlinear damping [49,50], including under interaction of the system with the non-ideal energy source considered in this paper.

Compared with the previously proposed centrifuge model [19,53], the improved viscoelastic support design replaces the rigidly fixed corrugated rubber support [19,53] with rubber plates in the form of a rectangular parallelepiped. These elements are installed in six (or eight) slots of the support structure and bear against the coupling. The rotor shaft rotates freely in a bearing mounted in the coupling.

The proposed design is distinguished by its simplicity, the possibility of rapid replacement of the viscoelastic elements with analogous materials having different elastic and damping characteristics, and the ability to vary the number and spatial arrangement of the rubber plates. Additional design features include replacing electromagnetic displacement and rotational-speed sensors with more accurate laser sensors, as well as using a computer-based system for control and recording of the measured parameters.

In Figure 24, the centrifuge comprises a platform 1, a housing 2, a cylindrical container 3, and a drive electric motor 4 rigidly mounted inside a cylindrical casing 5. The cylindrical casing 5 is connected to the platform 1 by a cardan joint 6. The shaft 7 of the electric motor 4 is connected to the housing 2 through a bearing (not shown in Figure 24) and a system of elastic damping inserts 8.

The elastic damping inserts 8 are made of a special grade of rubber or elastomer and are installed at the vertices of a regular hexagon (Figure 24b) or an octagon. An encoder 9 is installed at the lower part of the electric motor 4 to provide feedback to the control unit 10. To monitor the rotor motion characteristics, a vibration sensor 11 is mounted on the housing 2, and a laser rotational-speed sensor 12 is used to measure the rotational speed of shaft 7.

The developed device can operate both in the subcritical rotational-speed range (low-speed mode) and in the supercritical range (high-speed mode). The rotor speed is controlled by varying the supply voltage. In this case, the parameters of the rubber inserts 8 are selected so that the damping properties of the specially manufactured rubber or elastomer material prevent the occurrence of a jump phenomenon on the resonance curve caused by the nonlinear component of the elastic restoring force. This, in turn, makes it possible for the rotor to pass smoothly through the resonance region when selecting an operating rotational speed above the critical frequency.

 doi:10.20944/preprints202605.1561.v1

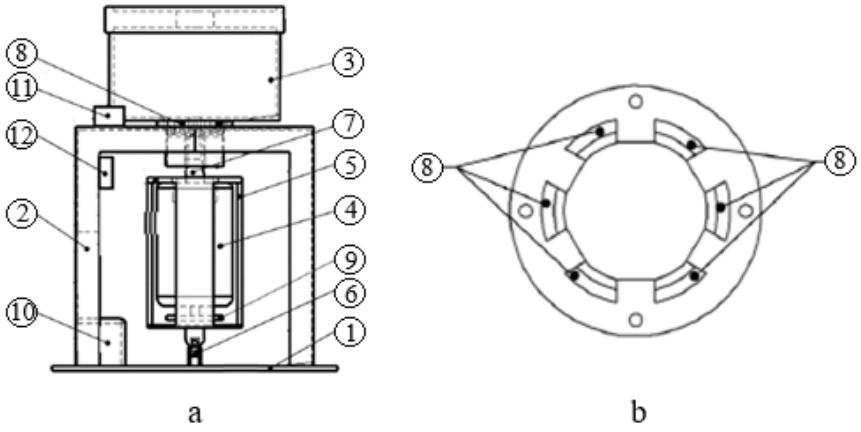

Figure 24. Schematic layouts of the centrifuge gyroscopic rotor and its viscoelastic support.

Supplementary Materials: The following supporting information can be downloaded at the website of this paper posted on Preprints.org and https://data.mendeley.com/datasets/5dx77dyz38/1, Video: Experimental setup of a centrifuge based on an anisotropic gyroscopic rotor in operation; https://data.mendeley.com/datasets/7xnd7y5w33/1, 3D Models: 3D Models of a Centrifuge Based on a Gyroscopic Rotor and Support Structure.

Author Contributions: Conceptualization, Z.I.; methodology, Z.I.; software, A.K.; validation, Z.I., A.J. and A.K.; formal analysis, Z.I., A.K.; investigation, Z.I., A.J. and A.K.; resources, Z.I., A.J. and A.K.; data curation, Z.I., A.K.; writing—original draft preparation, Z.I.; writing—review and editing, Z.I., A.J.; visualization, Z.I.; supervision, Z.I.; project administration, Z.I.; funding acquisition, Z.I. All authors have read and agreed to the published version of the manuscript.

Funding: This work was supported by the Science Committee of the Ministry of Science and Higher Education of the Republic of Kazakhstan (Grant No. BR31715767).

Data Availability Statement: Mendeley Data, Video. Available online: https://data.mendeley.com/datasets/5dx77dyz38/1, 3D Models. Available online: https://data.mendeley.com/datasets/7xnd7y5w33/1.

Conflicts of Interest: The authors declare no conflicts of interest.

References

1. Kononenko, V.O. *Vibrating systems with limited excitation*, 2rd ed.; Naukova dumka: Kiev, USSR, 1980; pp. 80–200, 36-48, 59-62.
2. Dimentberg, M.F.; McGovern, L.; Norton, R.L.; Chapdelaine J.; Harrison, R. Dynamics of an unbalanced shaft interacting with a limited power supply. *Nonlinear Dyn.* **1997,** *13 (2),* 171-187**.**
3. Samantaray, A.K.; Dasgupta S.S.; Bhattacharyya, R. Sommerfeld effect in rotationally symmetric planar dynamical systems. *Int. J. Engg. Sci.* **2010**, *48 (1),* 21-36. https://doi.org/10.1016/j.ijengsci.2009.06.005.
4. Ryzhik, A.T.; Amer, H.; Duckstein, L.; Sperling, L. Zum Sommerfeld effect beim selbsttätigen Auswuchten in einer Ebene. *Technische Mechanik* **2001,** *21 (4),* 297-312.
5. Quinn, D.D. Resonant dynamics in a rotodynamic system with nonlinear inertial coupling and shaft anisotropy. *Nonlinear Dyn.* **2009**, *57 (4)*, 623-633. https://doi.org/10.1007/s11071-009-9502-3.
6. Blekhman, I.I. *Vibrational Mechanics: Nonlinear Dynamic Effects. General Approach, Applications,* World Scientific, Singapore, 2000; pp. 99–137, 137–194, 158–194.
7. Goncalves, P.J.P.; Silvera, M.; Pontes, B.R. Numerical and experimental investigation of a vibration system with non-ideal vibration source. In Proceedings of the IX International Conference on Structural Dynamics, Porto, Portugal, June 30-July 02, 2014, pp. 2113-2117.
8. Balthazar, J.M.; Tusset, A.M.; Brasil, R.M.L.R.F.; Felix, J.L.P.; Rocha, R.T.; Janzen, F.C.; Nabarre, A.; Oliveira, C. An overview on the appearance of the Sommerfeld effect and saturation phenomenon in non-ideal

 doi:10.20944/preprints202605.1561.v1

vibrating systems (NIS) in macro and MEMS scales. *Nonlinear Dyn.* **2018**, *93*, 19-40. https://doi.org/10.1007/s11071-018-4126-0.

9. Vazquez, J.A.; Barrett, L.E.; Flak R.D. Flexible bearing supports, using experimental data. *J. Eng. Gas Turbines Power, Trans. ASME* **2002,** *124 (2)*, 369-374. https://doi.org/10.1115/1.1426085.
10. Gunter, E.J. The influence of internal friction on the stability of high-speed rotors. *J. Eng. Ind., Trans. ASME, Series B* **1967,** *89 (4)*, 683–688. https://doi.org/10.1115/1.3610135.
11. Tondl, A. *Some Problems of Rotor Dynamics*, Chapman and Hall: London, England, 1965; pp. 540–544.
12. Dimentberg, M.F. *Flexural Vibrations of Rotating Shafts,* Butterworths: London, England, 1961 pp. 150–162.
13. Lund, J.W. The stability of an elastic rotor in journal bearings with flexible, damped supports. *J. Appl. Mech.* **1965**, *32 (4)*, 911–920.
14. Bharti, S.K.; Bisoi, A.; Sinha, A.; Samantaray, A.K. Sommerfeld effect at forward and backward critical speeds in a rigid rotor shaft system with anisotropic supports. *J. Sound. Vib.* **2019**, *442*, 330-349. https://doi.org/10.1016/j.jsv.2018.11.002.
15. Bisoi, A.; Bharti, S.K.; Samantaray, A. K.; Bhattacharyya, R. Sommerfeld Effect Characterization in Anisotropic Non-ideal Rotor System. In *Book Advances in Rotor Dynamics, Control, and Structural Health Monitoring, Lecture Notes in Mechanical Engineering*, Dutta, S., et al., Eds.; Springer Nature Singapore Pte Ltd., 2020; Volume 3, pp. 51-61. https://doi.org/10.1007/978-981-15-5693-7_4.
16. Kafi, H.R.; Hosseini, S.A.A. Dynamic analysis of nonlinear rotating composite shafts excited by non-ideal energy source. *Zamm-Z. Angew. Math. Me.* **2019,** *99 (5).* https://doi.org/10.1002/zamm.201800279.
17. Bharti, S.K.; Sinha, A.; Samantaray, A.K.; Bhattacharyya, R. The Sommerfeld effect of second kind: passage through parametric instability in a rotor with non-circular shaft and anisotropic flexible supports. *Nonlinear Dyn.* **2020,** *100 (4)*, 3171-3197. https://doi.org/10.1007/s11071-020-05681-9.
18. Jha, A.K.; Dasgupta, S.S. Attenuation of Sommerfeld effect in an internally damped eccentric shaft-disk system via active magnetic bearings. *Meccanica* **2019**, *54 (1-2)*, 311-320. https://doi.org/10.1007/s11012-018-00936-7.
19. Iskakov, Zh. Resonant Oscillations of a Vertical Unbalanced Gyroscopic Rotor with Nonlinear Characteristics. In Proceedings of the 14th IFToMM World Congress, Taipei, Taiwan, October 25 – 30, 2015, Volume 3, pp. 505 – 513. https://doi.org/10.6567/iftomm.14th.wc.os14.001.
20. Iskakov, Zh.; Bissembayev, K.; Jamalov, N. Resonance Vibrations of a Gyroscopic Rotor with Linear and Nonlinear damping and Nonlinear stiffness of the Elastic support in interaction with a Non-ideal Energy source. *Mech. Syst. Signal Pr.* **2022,** *170* 108773. https://doi.org/10.1016/j.ymssp.2021.108773.
21. Iskakov, Zh.; Jamalov, N.; Abduraimov, A. Nonstationary Resonant Oscillations of a Gyroscopic Rigid Rotor with Nonlinear Damping and Non-ideal Energy Source. In *Mechanisms and Machine Science, Proceedings of ASIAN MMS: Advances in Asian Mechanism and Machine Science*, Hanoi, Vietnam, 15-18 December 2021, Nguyen Van Khang, Nguyen Quang Hoang, Nguyen Quang Hoang, Eds.; Springer Nature Switzerland AG: Cham, Switzerland, 2022; Volume 113, pp. 755–763. https://doi.org/10.1007/978-3-030-91892-7_72.
22. Iskakov, Z.; Jamalov, N.; Abduraimov, A. Non-stationary Resonance Transition of the Gyroscopic Rigid Rotor with Nonlinear Damping and Non-ideal Energy Source. In *Mechanisms and Machine Science, Proceedings of IFToMM Italy: Advances in Italian Mechanism Science*, 2nd ed.; Vincenzo Niola, Alessandro Gasparetto, Giuseppe Quaglia, Giuseppe Carbone, Eds.; Springer Nature Switzerland AG: Cham, Switzerland, 7-9 September 2022, Naples, Italy, 2022; Volume 3, pp. 114–122. https://doi.org/10.1007/978-3-031-10776-4_14.
23. Iskakov, Zh.; Jamalov, N. Resonant vibrations of a non-ideal gyroscopic rotary system with nonlinear damping and nonlinear stiffness of the elastic support. *MethodsX* **2023**, *10*, 101993. https://doi.org/10.1016/j.mex.2022.101993.
24. Grobov, V.A. *Asymptotic methods for calculating bending vibrations of turbomachine shafts*, Publ. house of the Academy of Science of the USSR: Moscow, 1961; pp. 29-30.
25. Rocard, Y. *Dynamique générale des vibrations*, Masson: Paris, 1949; pp. 230–245.
26. Blekhman, I.I. Self-Synchronization of Vibrators of Some Vibrating Machines. *Engineering collection* **1953**, *16*; pp. 50–55.

 doi:10.20944/preprints202605.1561.v1

27. Vishnevsky, S.N. *Characteristics of motors in an electric drive,* Energy: Moscow, 1977; pp. 35–45.
28. Kononenko, V.O.; Korablev, S.S. Experimental Study of Resonance Phenomena During Centrifugal Excitation of Variable Forces. In *Proceedings of the Moscow Technological Institute of Light Industry*, 1959; Volume 14, pp. 154–196.
29. Warminski, J. Regular and chaotic vibrations of Van der-Mathieu oscillator with non-ideal energy source. *J. Theor. Appl. Mech.* **2002**, *2 (40)*, 415-433.
30. Iskakov, Zh.; Bissembayev, K.; Jamalov, N.; Kamal, A. Dynamic modeling of a non-ideal gyroscopic rotor system with nonlinear damping and nonlinear rigidity of an elastic support. *Adv. Mech. Eng.* **2022**, *14 (7)*, 1–31. https://doi.org/10.1177/16878132221108675.
31. Richards, C.M.; Singh, R. Experimental characterization of non-linear rubber isolators in a multi-degree-of-freedom system configuration. *J. Acoust. S. Am.* **1999**, *106*, 21–78. https://doi.org/10.1121/1.427268.
32. Ravindra, B.; Mallik, A.K. Performance of non-linear vibration isolators under harmonic excitation. *J. Sound. Vib.*, **1994**, *170*, 325-337. https://doi.org/10.1006/jsvi.1994.1066.
33. Ravindra, B.; Mallik, A.K. Role of nonlinear dissipation in soft Duffing oscillators. *Phys. Rev. E* **1994**, *49*, 4950-4953. https://doi.org/10.1103/PhysRevE.49.4950.
34. Trueba, J.L.; Rams, J.; Sanjuan, M.A.F. Analytical estimates of the effect of nonlinear damping in some nonlinear oscillators. *Int. J. Bifurc. Chaos* **2000**, *10*, 2257–2267. https://doi.org/10.1142/S0218127400001419.
35. Zaitsev, S.; Shtempluck, O.; Buks, E.; Gottlieb, O. Nonlinear damping in a micromechanical oscillator. *Nonlinear Dyn.* **2012**, *67*, 859–883. https://doi.org/10.1007/s11071-011-0031-5.
36. Elliot, S.J.; Ghandchi Tehrani, M.; Langley, R.S. Nonlinear damping and quasi-linear modelling. *Phil. Trans. R. Soc. A* **2015**, *373*, 20140402. https://doi.org/10.1098/rsta.2014.0402.
37. Amabili, M. Derivation of nonlinear damping from viscoelasticity in case of nonlinear vibrations. *Nonlinear Dyn.* **2019**, *97 (3)*, 1785-1797. https://doi.org/10.1007/s11071-018-4312-0.
38. Amabili, M. Nonlinear damping in nonlinear vibrations of rectangular plates: derivation from viscoelasticity and experimental validation. *J. Mech. Phys. Solids* **2018**, *118*, 275-292.
39. Iskakov, Zh.; Bissembayev, K. The nonlinear vibrations of a vertical hard gyroscopic rotor with non-linear characteristics. *Mech. Sci.* **2019**, *10*, 529–544. https://doi.org/10.5194/ms-10-529-2019.
40. Awrejcewicz, J.; Krysko, V.A. *Introduction to Asymptotic Methods*, Boca Raton Fla, by Chapman and Hall/CRC Press, 2006; pp. 47–65, 66–80. https://lib.ugent.be/catalog/rug01:001020130.
41. Cveticanin, L.; Zukovic, M.; Cveticanin, D. Two degree-of-freedom oscillator coupled to a non-ideal source. *Int. J. Non. Lin. Mech.* **2017**, 94, 125–133. https://doi.org/10.1016/j.ijnonlinmec.2017.03.002.
42. Karthikeyan, M.; Bisoi, A.; Samantaray, A.K.; Bhattacharyya, R. Sommerfeld effect characterization in rotors with non-ideal drive from ideal drive response and power balance. *Mech. Mach. Theory* **2015**, 91, 269–288. https://doi.org/10.1016/j.mechmachtheory.2015.04.016.
43. Bisoi, A.; Samantaray, A.K.; Bhattacharyya, R. Sommerfeld Effect in a Gyroscopic Overhung Rotor-disk System. *Nonlinear Dyn.* **2018**, 88 (3), 1565–1585. https://doi.org/10.1007/s11071-017-3329-0.
44. Iskakov, Zh.; Bissembayev, K.; Jamalov, N.; Abduraimov, A. Modeling the Dynamics of a Gyroscopic Rigid Rotor with Linear and Nonlinear Damping and Nonlinear Stiffness of the Elastic Support. *Machines* **2021**, 9 (11), 276. https://doi.org/10.3390/machines9110276.
45. Iskakov, Zh.; Abduraimov, A.; Kamal, A. Dynamic Simulation of Gyroscopic Rigid Rotor with Anisotropy of Elastic Support Restoring and Damping Characteristics. In *Mechanisms and Machine Science, Proceedings of The Sixth Conference on Mechanisms, Transmissions and Applications - MeTrApp 2023, Futuroscope-Poitiers, France, 24-26 May 2023*, Laribi, M.A., Nelson, C. A., Ceccarelli, M., Zeghloul, S. Eds.; Springer Nature Switzerland AG: Cham, Switzerland, 2023; Volume 124, pp. 339–348. https://doi.org/10.1007/978-3-031-29815-8_32.
46. Iskakov, Zh.; Kamal, A.; Abduraimov, A.; Makhmutov, B. The Sommerfeld Effect in a Non-ideal Anisotropic Gyroscopic Rotor System and the Effect of Nonlinear Damping. In *Mechanisms and Machine Science, Proceedings of the 16th IFToMM World Congress (WC2023) -Volume 1: Advances in Mechanism and Machine Science, Tokyo, Japan, 6-9 November 2023*, Takeda, Yukio Ed.; Springer Nature Switzerland AG: Cham, Switzerland, 2023; Volume 147, pp. 846–856. https://doi.org/10.1007/978-3-031-45705-0_82.

 doi:10.20944/preprints202605.1561.v1

47. [dataset] Iskakov, Zharilkassin; Kamal, Aziz (2026), "Experimental setup of a centrifuge based on an anisotropic gyroscopic rotor in operation", Mendeley Data, V1, https://data.mendeley.com/datasets/5dx77dyz38/1.
48. ZETLAB Company. Available online: www.zetlab.com . Accessed on 22 June. 2025.
49. Abduraimov, A.; Iskakov, Z.; Kama,l A.; Kalybayeva, A. Gyroscopic rotor dynamics simulation with anisotropy of elastic and damping characteristics of the support. *Adv. Mech. Eng.* **2024**, 16 (9), 1–20. https://doi.org/10.1177/16878132241272189.
50. Abduraimov, A.; Iskakov, Zh.; Bissembayev, K..; Jamalov, N. Experimental Research of an Anisotropic Gyroscopic Rotor with Non-linear Elastic and Damping Characteristics of the Support. In *Mechanisms and Machine Science, Proceedings of the Asian MMS 2024: Advances in Asian Mechanism and Machine Science*, Almaty, Kazakhstan, 28-30 August, 2024; Tuleshov, A., Jomartov, A., Ceccarelli, M., Eds.; Springer Nature Switzerland AG: Cham, Switzerland, 2024; Volume 167, pp. 82–89. https://doi.org/10.1007/978-3-031-67569-0_10.
51. [dataset] Iskakov, Zharilkassin; Kamal, Aziz (2026), "3D Models of a Centrifuge Based on a Gyroscopic Rotor and Support Structure", Mendeley Data, V1, https://data.mendeley.com/datasets/7xnd7y5w33/1.
52. Iskakov, Zh.; Tuleshov, A.; Jamalov, N.; Kamal, A.; Abduraimov, A. Centrifuge Based on a Gyroscopic Rotor. *Eurasian Patent* 041048 B1, published 31 August 2022.
53. Iskakov, Zh.; Kunelbayev, M. Centrifuge Based on a Gyroscopic Rotor. *Kazakhstan Patent* KZ 32666 B, published 19 February 2018.